Evapotranspiration estimates in a traditional irrigated area in semi-arid Mediterranean. Comparison of four remote sensing-based models

Jamal Elfarkh, Vincent Simonneaux, Lionel Jarlan, Jamal Ezzahar, Gilles Boulet, Adnane Chakir, Salah Er-Raki

Evapotranspiration estimates in a traditional irrigated area in semi-arid Mediterranean. Comparison of four remote sensing-based models

Jamal Elfarkh[1,2], Vincent Simonneaux[3], Lionel Jarlan[3], Jamal Ezzahar[4,5], Gilles Boulet[3], Adnane Chakir[6], Salah Er-Raki[1,5]

(1) ProcEDE/AgroBiotech center, Département de Physique Appliquée, Faculté des Sciences et Techniques, Université Cadi Ayyad, Marrakech, Maroc
(2) Hydrology, Agriculture and Land Observation Group, Water Desalination and Reuse Center, Biological and Environmental Science and Engineering Division, King Abdullah University of Science and Technology, Thuwal, Saudi Arabia
(3) Centre d'Etudes Spatiales de la BIOsphère, CESBIO, Toulouse University, CNRS, CNES, IRD, UPS, INRAE, Toulouse, France
(4) Département IRT, Laboratoire MISCOM, Ecole Nationale des Sciences Appliquées, Université Cadi Ayyad, Safi, Maroc
(5) Mohammed VI Polytechnic University (UM6P), Morocco, Center for Remote Sensing Applications (CRSA)
(6) LMFE, Département de Physique, Faculté des Sciences Semlalia, Université Cadi Ayyad, Marrakech, Maroc

Keywords: Evapotranspiration modelling, Remote sensing, Energy balance, FAO-56, Irrigation

Research Highlights

- Four crop evapotranspiration estimates approaches based on remote sensing were compared
- Eddy-Covariance and Scintillometer measurements were used for models' assessment
- The four models estimate correctly the seasonal variations of actual crop ET
- FAO-56 and METRIC GEE show the best results over a mixed irrigated area

Abstract

Quantification of actual crop evapotranspiration (ETa) over large areas is a critical issue to manage water resources, particularly in semi-arid regions. In this study, four models driven by high resolution remote sensing data were intercompared and evaluated over an heterogeneous and complex traditional irrigated area located in the piedmont of the High Atlas mountain, Morocco, during the 2017 and 2018 seasons: (1) SAtellite Monitoring of IRrigation (SAMIR) which is a software-based on the FAO-56 dual crop coefficient water balance model fed with Sentinel-2 high-resolution Normalized Difference Vegetation Index (NDVI) to derive the basal crop coefficient (K_{cb}); (2) Soil Plant Atmosphere and Remote Sensing Evapotranspiration (SPARSE) which is a surface energy balance model fed with land surface temperature (LST) derived from thermal data provided from Landsat 7 and 8; (3) a modified version of the Shuttleworth–Wallace (SW) model which uses the LST to compute surface resistances and (4) METRIC-GEE which is a version of METRIC model ("Mapping Evapotranspiration at high

Resolution with Internalized Calibration") that operates on the Google Earth Engine platform, also driven by LST. Actual evapotranspiration (ETa) measurements from two Eddy-Covariance (EC) systems and a Large Aperture Scintillometer (LAS) were used to evaluate the four models. One EC was used to calibrate SAMIR and SPARSE (EC1) which were validated using the second one (EC2), providing a Root Mean Square Error (RMSE) and a determination coefficient (R) of 0.53 mm/day (R=0.82) and 0.66 mm/day (R=0.74), respectively. SW and METRIC-GEE simulations were obtained respectively from a previous study and Google Earth Engine (GEE), therefore no calibration was performed in this study. The four models predict well the seasonal course of ETa during two successive growing seasons (2017 and 2018). However, their performances were contrasted and varied depending on the seasons, the water stress conditions and the vegetation development. By comparing the statistical results between the simulation and the measurements of ETa it has been shown that SAMIR and METRIC-GEE are the less scattered and the better in agreement with the LAS measurements (RMSE equal to 0.73 and 0.68 mm/day and R equal to 0.74 and 0.82, respectively). On the other hand, SPARSE is less scattered (RMSE = 0.90 mm/day, R = 0.54) than SW which is slightly better correlated (RMSE = 0.98 mm/day, R = 0.60) with the observations. This study contributes to explore the complementarities between these approaches in order to improve the evapotranspiration mapping monitored with high-resolution remote sensing data.

1 Introduction

The Mediterranean region suffers from drought and increasing depletion of water resources due to the effect of climate change and of the increasing anthropic water demand (Le Page et al., 2012). However, agricultural production continues to increase and is the largest consumer of available water resources (Boukhari et al., 2015). In order to achieve a balance between agricultural production and water availability, a good monitoring of the crop hydric conditions is necessary. Numerous studies have been conducted on the measurement and estimation of the water balance components of the crops in the semi-arid region of Tensift Al Haouz but most of these studies were carried out in the plain (Amazirh et al., 2017; Aouade et al., 2020; Diarra et al., 2017; Er-Raki et al., 2010; Ezzahar et al., 2007a; Ait Hssaine, Merlin, et al., 2018; Ouaadi et al., 2020; Rafi et al., 2019). By contrast, the mountain foothills in semi-arid regions are potential recharge areas for the groundwater table (Blasch & Bryson, 2007; Bouimouass et al., 2020; Liu & Yamanaka, 2012; Martinez et al., 2017). This recharge is poorly known but could be quantified by residual balance term. However, the uncertainty on the water balance variables in these regions such as the precipitation and evapotranspiration (ET) increase the uncertainty on the estimation of recharge. Hence there is a need for an accurate estimate of ET. In the last decades, a number of studies focused on developing several methods for measuring and estimating ETa based on remote sensing that provides valuable data to assess its spatial and temporal variation.

There is a variety of methods allowing direct or indirect ETa measurement in the field with variable spatial and temporal representativeness (Allen et al., 2011; Er-Raki et al., 2013). The most used methods are the lysimeter (Sánchez et al., 2019; Widmoser & Wohlfahrt, 2018) and the eddy covariance system (Anapalli et al., 2020; Fang et al., 2020), both provide typically hectometric scale measurements, and the scintillometer allowing measurements over transects of several kilometers (Duchemin et al., 2008; Elfarkh et al., 2020; Ezzahar et al., 2007a; 2007b; 2009a; 2009b; 2009c; Isabelle et al., 2020; Zhao et al., 2018). While these devices are the most accurate way to measure ET, their use over large areas is limited due to their cost and their limited spatial representativity, especially in Mediterranean landscapes known by heterogenous crops and water status. Major efforts to develop methods for ETa mapping have been undertaken during the last decades, particularly with the development of remote sensing data providing land surface characteristics using multi-spectral data from optical bands. The most physical approaches are based on Soil-Vegetation-Atmosphere Transfer (SVAT) models, coupling the soil water balance and the surface energy balance for soil-plant-atmosphere system and to quantify the amount of ETa released in the atmosphere (Montes et al., 2014). These models offer an accurate estimates of ETa but are complex because in addition to meteorological forcing (i.e., air temperature and humidity, wind speed, incident radiation, rainfall), they require a large number of parameters such as information on vegetation structure (i.e., leaf area index, LAI, height) and vegetation functioning (i.e., stomatal conductance), on thermal and hydraulic properties of the soil (Olioso et al., 1999). To overcome these constraints, simplified water balance models have been proposed like the FAO-56 dual crop coefficient approach (Allen et al., 1998). This model requires a lower number of parameters and some of the main ones, the crop coefficients, can be related to the amount of active vegetation present in the surface so that they can be estimated from remote sensing using vegetation indices. On the other hand, another category of ETa estimation method is based on the surface energy balance (SEB). SEB type models are usually constrained by satellite land surface temperature observations, which are considered as a good indicator of the water status of the surface, allowing to take into consideration the stress condition in estimating actual ET. They calculate the sensible heat flux (H) from which the latent heat flux (LE) associated with ETa is estimated as a residual term of the energy balance equation (Chirouze et al., 2014). These models are a good indicator of the crop water status, but they basically provide instantaneous estimates of ETa at the time of the satellite acquisition. SEB models can be divided into two levels of complexity (Li et al., 2009): 1) single-source models that consider the surface as a big leaf (Allen et al., 2007; Bastiaanssen et al., 1998; Roerink et al., 2000; Su, 2002) and 2) dual-source models distinguishing between soil and vegetation processes (Anderson et al., 1997; Boulet et al., 2015; Norman et al., 1995). Numerous authors have compared these two approaches, showing that dual-source models show better performance over sparse vegetation. However, several authors have also found that with a correct calibration even a single-source model can properly simulate the energy fluxes (Bastiaanssen et al., 1998; Kustas & Norman, 1996).

The main objective of this study was to test the performance of different approaches used for estimating ETa over a heterogeneous landscape of traditional irrigated agriculture in a semi-arid area located in the piedmont of the High Atlas Mountains (Morocco). A simplified water balance model SAMIR (Simonneaux et al., 2009), SPARSE model (Boulet et al., 2015), the modified Shuttleworth-Wallace model (Elfarkh et al., 2021) and METRIC model (Allen et al., 2007) were compared during two seasons, 2017 and 2018. This study is a preliminary step to build an hybrid approach that could benefit from both the continuity of water budget based estimates and the accuracy of thermal based ones.

2 Material and methods

2.1 Study area

The experiment was carried out over the piedmont of the High Atlas Mountain near the Marrakech city in the center of Morocco (31°22'1.19"N, 7°56'47.21"O) (Figure 1). The climate in this area is semi-arid with irregular and low rainfall especially during the study period with a total rainfall of 157 mm for 2017 and 384 mm for 2018. The study site is characterized mainly by traditional olive trees of various ages, with some other species (apple, apricot, plum, orange, peach, ETa) and a frequent understory of annual crops below the trees, mainly cereals. Crops are irrigated by the traditional flooding technique using water diverted from the river issued from the mountains. Some patches of bare soils are also present especially at the surrounding of the irrigated area.

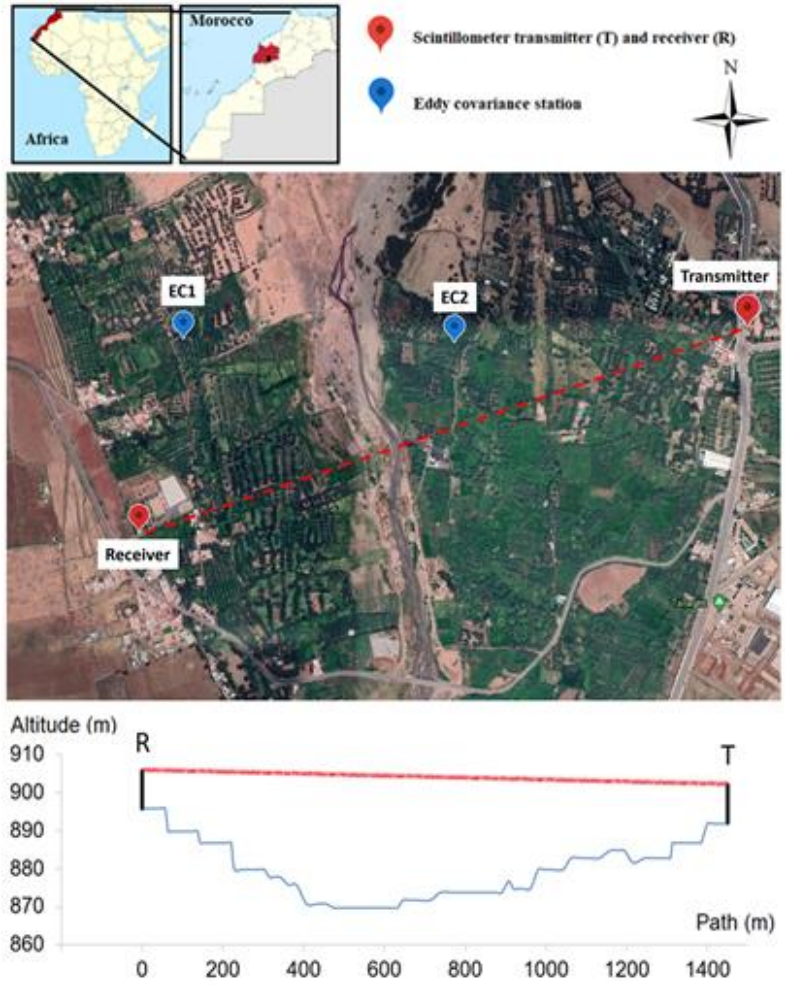

Figure 1: Eddy covariance and the scintillometer stations superimposed on an image of the study site from Google Earth. The plot at the bottom shows the scintillometer path and elevation along the path

2.2 Experimental data

Both EC stations (EC1 and EC2) were equipped by meteorological instruments to measure the net radiation components (CNR4 radiometer, Campbell scientific) at a height of 17 m, air temperature and humidity (Vaisala HMP155, Campbell scientific) at height of 16 m (Figure 1). Also, the soil heat flux was measured at a depth of 5 cm using two heat flux plates (HPF_01, Campbell Scientific), one shaded by trees and the other one exposed to solar radiation. The rainfall was recorded using a rain gauge (ARG100/EC) installed close to the scintillometer receiver (Figure 1).

Flux stations were installed during 2017 and 2018 over two olive tree plots located in the study area on 17.5 m height towers (EC1 and EC2 sites) (Elfarkh et al., 2020). The land cover of these two sites is supposed to be representative of the entire site, namely traditional olive plantations of 7 to 10 meters height with an understory of herbaceous vegetation, mainly wheat. EC2 shows more heterogeneity than EC1 since it includes olive trees, other fruit trees (mainly apple trees) and annual crops (Elfarkh et al., 2020). They measured the sensible and latent heat fluxes using the eddy correlation method, consisting of a 3D sonic anemometer (CSAT3, Campbell Scientific Ltd.) and a Krypton hygrometer (KH20,

Campbell Scientific Ltd.). The raw data were sampled at a rate of 20Hz and then used to calculate sensible (H) and latent (LE) heat fluxes offline using the EC processing software 'ECpack' (Van Dijk et al. 2004). The energy balance closure analysis showed that the sum of the turbulent fluxes only reaches 60% of the available energy (Elfarkh et al., 2020) which can be considered acceptable due to the complexity of the study sites. Therefore, the correction of EC data was performed using the approach suggested by Twine et al. (2000), which assumes the non-closure energy balance is due to underestimates from EC measurements while the corresponding Bowen ratio (H/LE) is correctly estimated. However, the reliability of ETa after this correction still affected by some uncertainty given the assumptions taken in the Bowen correction namely the assumption that the difference between the net radiation (Rn) and the soil heat flux (G) is equal to the sum of H and LE neglecting the energy stored in the canopy. In addition, the footprint of the devices that measure both energy quantity Rn-G and H+LE are different and that can generate an error especially in heterogeneous areas such as our study site.

In addition to the EC towers, a Large Aperture Scintillometer (LAS) was installed over a 1464 m transect, consisting of a receiver installed on a tower of about 10 m and a transmitter over a building of about 10.5 m in the city (Elfarkh et al., 2020). Due to topography, the height between the LAS path and the ground varied between 10 and 50 m and the effective height computed was around 26 m (Hartogensis et al., 2003). The measurement of the refraction phenomena produced by the air turbulence allow the calculation of the variation of the structure parameter of the refractive index C_n^2 along the path (Wesely, 1976). The sensible heat flux (H) was calculated iteratively based on the Monin-Obukhov theory (De Bruin et al., 1993). The latent heat flux (LE) was obtained as the residual term of the energy balance, where available energy was computed from the ground measurements (Elfarkh et al., 2020). For the LE computation, we used the Rn and G measured at the EC1 site which is considered representative of the land cover present in the LAS footprint. However, this remains an approximation and one possible improvement would be to multiply measurements of Rn and G along the LAS path but this is operationally difficult to achieve. For the sake of simplicity, we also didn't compute MODIS estimates of daily Rn (Saadi et al., 2015).

2.3 Remote sensing data

2.3.1 Sentinel-2 data

The Normalized Difference Vegetation Index (NDVI) was computed using Sentinel-2 Red (R, band 4) and Near-InfraRed (NIR, band 8) reflectances at 10 meters resolution (Eq. 1). The Sentinel-2 images were downloaded from the THEIA web site, a French open-source land data service center (https://www.theia-land.fr/) providing cloud-free and atmospherically corrected surface reflectance images. NDVI is closely related to vegetation cover (Tucker, 1979). Sentinel 2 images have the advantage of constant viewing angles, limiting its impact on the same site. In addition, as images used

were radiometrically corrected, the effect of atmosphere was very limited. Although NDVI saturates regarding leaf area index (LAI), this is less of a problem regarding crop coefficient, which also saturates with LAI due to shading effect. As a result, it has been shown in many studies that crop coefficient can be linearly related to NDVI (Choudury et al., 1994). This index has been widely used in the region of our study area to characterize vegetation development and crop coefficients (Amazirh et al., 2022; Rafi et al., 2019; Duchemin et al., 2006; Er-Raki et al., 2007, 2010).

$$NDVI = \frac{NIR - R}{NIR + R} \quad \text{Eq: 1}$$

2.3.2 Landsat data

Both Landsat 7 and 8 satellites data were used in this study for the period 2017 and 2018 with a revisit time up to 8 days thanks to their shifted overpasses. The area is located in the center of the Landsat 7 scene not affected by the SLC-off problem. Land Surface Temperature (LST) data was acquired from the web application (http://rslab.gr/downloads_LandsatLST.html) developed by Parastatidis et al. (2017). This application provides LST estimates using the single channel algorithm. The Landsat LST values were compared to measurement values from the CNR4 instrument over both stations EC1 and EC2. This comparison displayed in Figure 2a shows acceptable agreement between measured and Landsat LST with an RMSE of about 5 K for EC1 and 6.6 K for EC2, with a moderate but significant bias. However, despite the good correlation between ground and satellite data, we chose not to correct satellite data considering the low representativity of our local measurements as compared to satellite pixels (30 m) in this heterogeneous land cover context. The optical Landsat bands were downloaded in level 2 from the web site (https://earthexplorer.usgs.gov/) with atmospheric correction included.

Surface emissivity, albedo and the leaf area index (LAI) were computed using the optical Landsat data. The surface emissivity was calculated based on Tardy et al. (2016) as follows:

$$\varepsilon = \varepsilon_v - (\varepsilon_v - \varepsilon_s)\left(\frac{NDVI - NDVI_{max}}{NDVI_{min} - NDVI_{max}}\right)^k \quad \text{Eq: 2}$$

ε_v and ε_s are the soil and the vegetation emissivity. Their values are 0.96 and 0.99 respectively (Sobrino et al., 2004; Tardy et al., 2016). The $NDVI_{min}$ is the minimum value of NDVI representing bare soil and the $NDVI_{max}$ is the maximum value of NDVI representing dense vegetation, determined by examination of the images NDVI distribution. The k parameter was fixed arbitrarily to 2 according to Tardy et al. (2016). LAI was computed based on Landsat NDVI following (Wang et al., 2008):

$$LAI = \sqrt{NDVI\frac{1 + NDVI}{1 - NDVI}} \quad \text{Eq: 3}$$

The visible and the near-infrared bands are used to retrieve the albedo (α) from Landsat data. The best combinations compared to in-situ measurement were obtained from the Red (R) and the Near-InfraRed (NIR) bands which is in-line with results obtained with other sensors including SPOT4 (Diarra et al., 2017) and FORMOSAT (Courault et al., 2008).

$$\alpha = 4.16 * 10^{-5} * R + 3.28 * 10^{-5} * NIR \qquad for\ Landsat\ 7 \qquad \text{Eq: 4}$$

$$\alpha = 2.72 * 10^{-5} * R + 3.80 * 10^{-5} * NIR \qquad for\ Landsat\ 8 \qquad \text{Eq: 5}$$

Figure 2b shows a large discrepancy between measured and estimated albedo. The errors can be explained by the high heterogeneity of the pixel area while point-scale albedo is measured by the stations. As long as the regression linear equation obtained from satellites data was not good, a fixed value of about 0.12 was adopted for the study site.

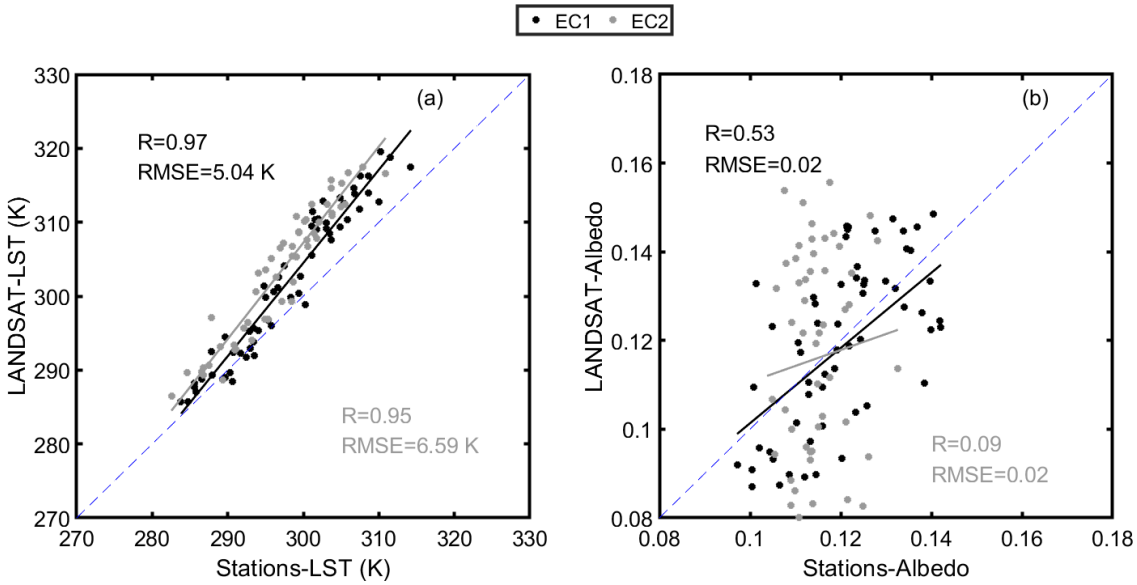

Figure 2: Scatterplot of Landsat LST (a) and albedo (b) versus in-situ data for EC1 and EC2 stations.

2.4 Evapotranspiration Modeling

Four models are used in this study. SAMIR is a software simulating crop water budget and evapotranspiration at daily scale based on the FAO-56 approach. It is fed with Sentinel-2 Normalized Difference Vegetation Index (NDVI) images used to compute both the basal crop coefficient (K_{cb}) and the vegetation fraction cover (fc). A soil water budget allows to automatically trigger irrigations based on simulated soil moisture. The SPARSE model solves the surface energy budget to provide instantaneous latent heat flux (LE) estimates using the Landsat 7 and 8 thermal data. Both models were tested over different crops and climates and have shown acceptable performance in estimating ETa (Boulet et al., 2015; Delogu et al., 2018; Saadi et al., 2015; Simonneaux et al., 2009). The Shuttleworth-Wallace and METRIC models have been added to this study to enrich the comparison of different approaches to estimating ETa using the same input data. For the Shuttleworth-Wallace model the version

used here is the modification proposed by Elfarkh et al., (2021) where they use thermal remote sensing data to spatialize ET. SPARSE, SW and SAMIR were calibrated and validated over the same study area using eddy covariance and scintillometer measurements. Regarding METRIC, its automated version featured on the Google Earth Engine Evapotranspiration Flux (EEFlux) platform is used. More details on each model are presented in the appendix. A summary of the inputs required and the parameters calibrated for each model is depicted in table 1.

Table 1: Summary table of the inputs required and the parameters calibrated for each model.

Models	Inputs variables	Calibrated parameters	Calibration approach
SPARSE	- NDVI and Albedo - LST and emissivity - Air temperature and humidity - Wind speed - Solar radiation	- Minimum stomatal resistance (rst_{min}) - Leaf width (w) - Ratio relating the soil net radiation to the heat soil flux (ξ) - Extinction coefficient (k) in the LAI equation - Coefficient in the aerodynamic resistance (n_{SW})	- Minimization of the RMSE between the estimated and measured ETa
SAMIR	- NDVI - ET_0 - Rainfall	- NDVI-K_{cb} relation's slope - NDVI-K_{cb} relation's intercept - Readily evaporable water (REW) - Maximum root depth (Zr_{max}) - Water diffusion coeff. between surface and root layers (Dif_{er})	- Minimization of the RMSE between the estimated and measured ETa
SW	- NDVI and Albedo - LST and emissivity - Air temperature and humidity - Wind speed - Solar radiation	- Coefficients in the soil and vegetation resistances	- Minimization of the RMSE between the estimated and measured ETa
METRIC-GEE	- NDVI and Albedo - LST and emissivity - Air temperature and humidity - Wind speed - Solar radiation	- No calibration	

2.5 Models evaluation

The evaluation of results was achieved using standard criteria, namely the correlation coefficient (R), the bias and the root mean square error (RMSE).

$$R = \frac{\sum(x_i - \overline{x})\,(y_i - \overline{y})}{\sqrt{\sum(x_i - \overline{x})^2 \sum(y_i - \overline{y})^2}} \quad \text{Eq: 6}$$

$$bias = \frac{1}{n}\sum_{i=1}^{n}(y_i - x_i) \quad \text{Eq: 7}$$

$$RMSE = \sqrt{\frac{1}{n}\sum_{i=1}^{n}(y_i - x_i)^2} \quad \text{Eq: 8}$$

where x_i is the measured values, y_i is the estimated values and n is the number of observations.

2.6 Extrapolation of instantaneous ETa to daily value

Thermal remote sensing-based ETa models like SPARSE and SW basically provide an instantaneous ETa value at the satellite overpass time. However, these instantaneous values are not useful for practical purposes which support water resources management such as irrigation scheduling. Many authors evaluated different temporal upscaling methods from instantaneous to daily ETa values (Xu et al., 2015; Saadi et al., 2018). One of the methods widely used is the evaporative fraction (EF). This latter supposes that the evaporative fraction remains almost constant during the day. However, Gentine et al. (2007) reported that EF depends on soil moisture and is not always satisfied for a fully vegetated surface. Here, we applied the method parametrized by Delogu et al. (2012) based on an improvement of EF method. This improvement is based on the diurnal variations of EF derived by Hoedjes et al. (2008) using an empirical relationship. This relation parameterized EF diurnal trend as a function of incoming solar radiation and relative humidity as follows.

$$LE_{day} = EF * AE_{day} \quad \text{Eq: 9}$$

$$AE_{day} = AE_{inst} * \frac{Rg_{day}}{Rg_{inst}} \quad \text{Eq: 10}$$

$$EF = \left(1.2 - \left(0.4\frac{Rg_{day}}{1000} + 0.5\frac{RH_{day}}{100}\right)\right) * \frac{EFsat_{inst}}{EFbase_{inst}} \quad \text{Eq: 11}$$

$$EFsat_{inst} = \frac{LE_{inst}}{AE_{inst}} \quad \text{Eq: 12}$$

$$EFbase_{inst} = 1.2 - \left(0.4\frac{Rg_{inst}}{1000} + 0.5\frac{RH_{inst}}{100}\right) \quad \text{Eq: 13}$$

where AE is the available energy ($Rn - G$), Rg is the solar radiation (W/m^2), RH is the relative humidity, EF is the evaporative fraction and $EFsat_{inst}$ and $EFbase_{inst}$ are the evaporative fraction observed at the satellite overpass time and calculated at the satellite overpass with the first part of the Eq. 11, respectively.

2.7 Footprint computation

The LAS or EC measurements are influenced by an area, or footprint, where the contribution of each point is determined by its position, the wind speed and direction. Numerous models of footprint have been developed (Horst & Weil, 1992; Rannik et al., 2000; Schuepp et al., 1990). In our case, Horst and Weil (1992) model was used for the EC measurements, where the measured F flux is related to the surface elementary fluxes distribution (Eq. 14).

$$F(x, y, z_m) = \int_{-\infty}^{\infty}\int_{\infty}^{x} F_0(x', y') f(x - x', y - y', z_m) dx' dy' \quad \text{Eq: 14}$$

where f is the footprint function figuring the spatial weighting of elementary surface fluxes, $F(x, y, (z = 0)) = F_0(x, y)$. x and y are the downwind and crosswind distances (m) from the measurement's points, respectively. For the LAS, the spatial weighting function is used to weight each point (Meijninger, 2003) (Eq. 15).

$$F_{LAS}(x, y, Z_{LAS}) = \sum_{i=1}^{N} F(x, y, Z_{LAS}) G(d_i) \quad \text{Eq: 15}$$

where $F_{LAS}(x, y, Z_{LAS})$ is the LAS integrated measurement, and $F(x, y, Z_{LAS})$ and $G(d)$ are the equivalent EC footprint and the scintillometer path-weighting function, respectively, for a given point distanced from the transmitter by d_i. The EC and LAS footprints were calculated for each half-hour (Figure 3a). To compare the measured flux with daily model outputs, daily footprints were calculated as the sum of the half-hourly footprints weighted by the net radiation values. As shown on the figure 3b, the daily footprint has a more complex form than the instantaneous ones because half-hourly footprints have different direction and form depending on the wind.

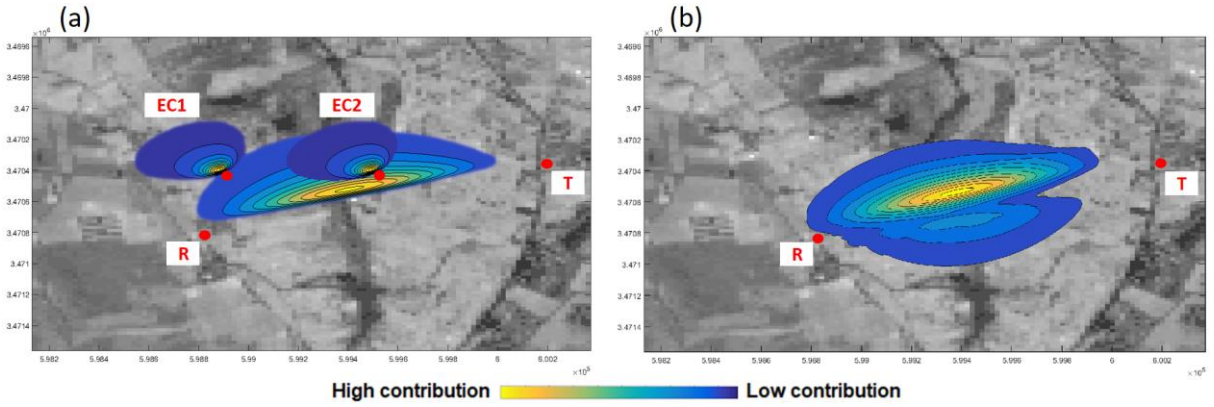

Figure 3: (a) Instantaneous footprint of both stations (EC1 and EC2) and LAS, (b) daily LAS footprint. R and T means the receiver and the transmitter of scintillometer, respectively.

3 Results

In this section the ETa estimations by the four models are presented. Only the calibration and the validation of SAMIR and SPARSE are shown here. The calibration of SW is detailed over the same site in Elfarkh et al. (2021). METRIC is downloaded from a Google Earth Engine platform. After that, the four models' estimations are evaluated and compared with the LAS and the EC measurements and the errors and domains of validity are discussed.

3.1 SAMIR calibration

The main parameters of SAMIR are basically related to crop types and to the soil. Thus, a land cover map of the study area was generated from the NDVI time series using the algorithm developed by Simonneaux et al., (2007). The main classes were trees, annual crops and bare soil. A Sentinel-2 NDVI time series was extracted by averaging pixel values in a 50*50 meters area centered on the EC1 site. The meteorological forcing, namely precipitation and ET_0 were obtained from our in-situ measurements. The SAMIR model was calibrated for the tree class using latent heat flux measured over EC1 for the two seasons 2017 and 2018, through minimizing the Root Mean Square Error (RMSE) computed between measured and modeled ET. The main calibrated parameters are listed in table 2. The rooting depth (Zr_{max}) obtained after calibration (4.9 m) is much larger than usual values proposed in the FAO-56 paper (1.6 m) for irrigated olive trees. This is not surprising considering that these trees are very old and periodically under stress, which causes deep rooting. The olive tree root system is adapted to water scarcity frequent in the mediterranean areas (Fernández 2014). In aerated soils of light texture, olive trees roots may reach depths of 7 m (Lavee, 1996). For the annual crops, no calibration was possible since no EC station was installed over such class. Instead, we used the parameters obtained by Saadi et al. (2015) after calibration of SAMIR over wheat plots in central Tunisia that we consider similar to our site. Irrigation was simulated assuming that the farmer avoid stress, triggering input just before stress and bringing the water amount required to fill the soil holding capacity. The irrigation simulations were

293 stopped from 16 July to 30 November 2017 and from 21 May to 26 September 2018, according to ground
294 observation.

295 *Table 2: Main Calibrated Parameters used for the tree class.*

Parameter	Definition	Value	Source
a_{fc}	NDVI-fc relation's slope	1.33	Satellite imagery
b_{fc}	NDVI-fc relation's intercept	-0.20	Satellite imagery
a_{Kcb}	NDVI-K_{cb} relation's slope (Eq. A.2)	1.35	Calibrated
b_{Kcb}	NDVI-K_{cb} relation's intercept (Eq. A.2)	-0.20	Calibrated
Ze (mm)	depth of the soil evaporation layer	125	FAO-56
REW (mm)	Readily evaporable water	0	Calibrated
m	Reduction coefficient (Torres et al. 2010)	0.185	Calibrated
Zr_{max} (mm)	Root depth (assumed constant for trees)	4900	Calibrated
p	root zone water depletion fraction before stress	0.65	FAO-56
Dif_{er}	Diffusion between surface and root layers	0	Calibrated
ω_{fc} (m^3/m^3)	Volumetric water content at field capacity	0.4	Ground observation
ω_{wp} (m^3/m^3)	Volumetric water content at wilting point	0.2	Ground observation
Kc_{max}	Maximum value of crop coefficient (following rain or irrigation) which is determined by the energy available for ETa at the soil surface	1.15	Ground observation

296

297 Figure 4 shows the temporal variations of the computed basal crop coefficient K_{cb} and the fraction cover
298 (fc) values using the NDVI relationships with NDVI averaged over the EC1 station. Peak K_{cb} and fc
299 values were observed at the beginning of spring for both years 2017 and 2018, while minimum K_{cb} and
300 fc values were recorded in summer and early autumn. These variations are linked to the vegetative cycle
301 of the olive tree itself, but they may be amplified by the understory of annual crops often observed in
302 this area in spring and early summer, when water is available from the river. Conversely, the K_e values
303 don't exhibit the same seasonality and are only linked to water inputs (irrigation or rainfall). It is
304 remarkable to note that the resistance to evaporation is much increased as compared to FAO standards,
305 with $REW = 0$ and m = 0.185, which is coherent with previous studies (Saadi et al., 2015; Torres &
306 Calera, 2010). Thus, K_e values are on the whole quite low (below 0.2), which can be explained by the
307 important canopy shading, modifying significantly the meteorological forcing at the soil level. The K_s
308 values show non-stressed conditions during vegetation developments (i.e., $K_s = 1$), while stress appears
309 in late summer and autumn justified by the insufficient irrigation due to water shortage in the river.

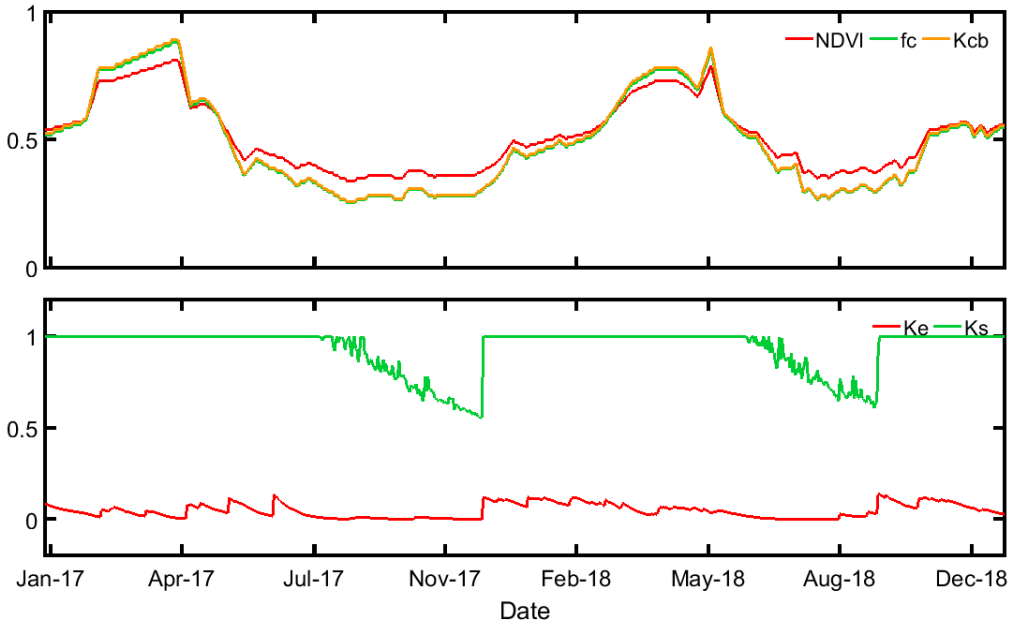

Figure 4: Simulation of the evaporative coefficient (K_e), the stress coefficient (K_s), the crop coefficient (K_{cb}) and the fraction cover (fc) during the study period 2017 and 2018, as obtained from SAMIR modelling on the EC1 site.

The SAMIR ETa simulations are in good agreement with observed values with an RMSE, bias and R of about 0.50 mm/day, -0.11 mm/day and 0.87, respectively (Figure 5). The simulated values reproduce well the seasonal cycle. During the development stage of wheat in spring, ETa was higher in the dry season (2017) than the wet one (2018) which is strongly related to the higher reference evapotranspiration in 2017. Despite the lack of rainfall, water is still available for irrigation in spring because water comes from the mountains and is not affected directly by drought occurring downstream. However, the gap between ETa and ET_0 during summer and autumn can be related to the water supply. This gap is large in 2017 when compared to 2018 since the first year is dry with 157 mm whereas 2018 is wetter with 384 mm. However, even in these stressed conditions, the olive trees managed to keep a high level of transpiration due to the deep rooting of the trees.

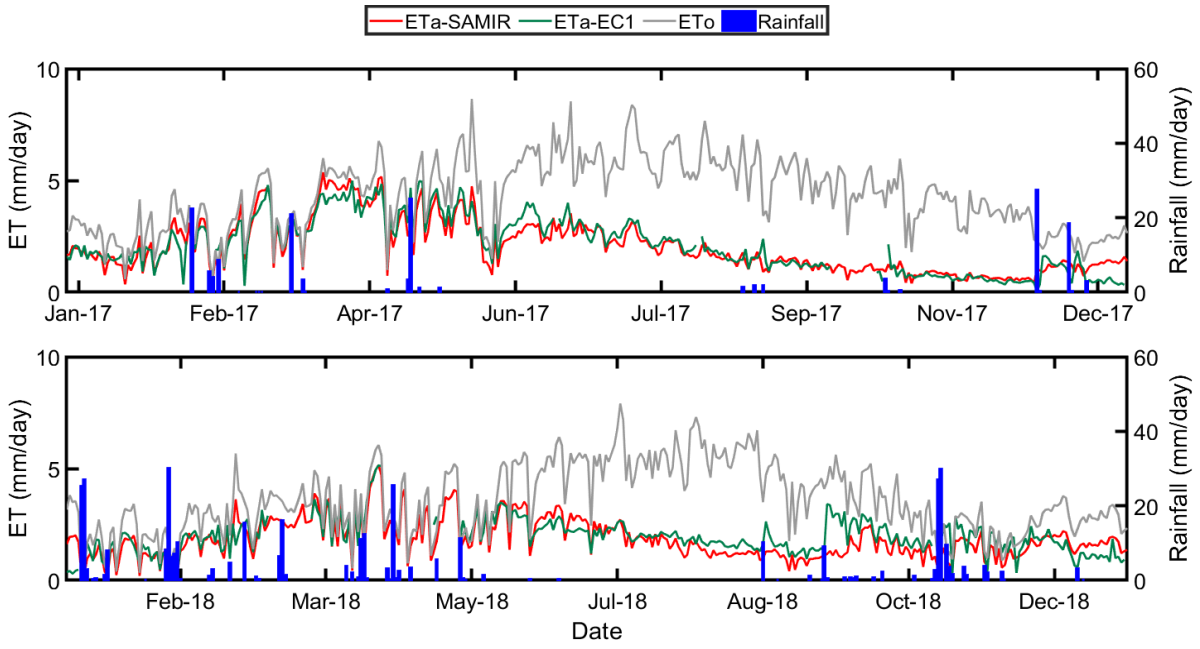

Figure 5: Daily ETa measured by EC1 and estimated over the EC1 footprint by SAMIR during the study periods 2017 and 2018.

3.2 SAMIR validation

Using the calibrated parameters (Table 1), SAMIR was run over the study area using the Sentinel-2 NDVI time series. The simulated SAMIR ETa values were validated using measurements provided by the EC2 and the LAS. For the latter, SAMIR daily ETa outputs were weighted according to the daily footprint computed as explained previously. The comparison between SAMIR daily ETa and ETa measured by EC2 in 2017 and 2018 shows a good agreement with an RMSE, bias and R of about 0.53 mm/day, -0.12 mm/day and 0.82 (Figure 6), very close to the values obtained during the calibration stage on EC1. However, in 2017 SAMIR overestimated ETa during the dry period from July to November. This is because a spatialized version of the SAMIR tools is used in this study and it doesn't allow to stop irrigation while no water is available at this time of the season. By contrast, no overestimation of ETa was observed in summer 2018, as the year was wet and there was less water shortage in the root zone despite the lack of irrigation.

The comparison between SAMIR daily ETa and the LAS measurements in 2017 and 2018 is presented on figure 7. Due to technical problems, the LAS measurements are lacking from June to August 2018. On average, a good concordance is noticed between the simulations and the measurements with an RMSE, bias and R of 0.73 mm/day, -0.45 mm/day and 0.74, respectively. However, between January and June 2017, SAMIR underestimated ETa. One possible explanation for this gap is that during this period, since there is enough rainfall and no stress, SAMIR doesn't apply any irrigation which is not the case for the farmers who do not hesitate to bring water when it is available in the river. Indeed, as shown by Bouimouass et al., (2020) who studied irrigation in a very similar watershed neighboring the study site, overirrigation is very frequent as is driven by water availability and not by the crop requirements.

In 2018, this discrepancy between simulated and measured ETa is also visible but to a lesser extent; possibly because the precipitation was relatively high and consequently the impact of irrigation on ETa was lower.

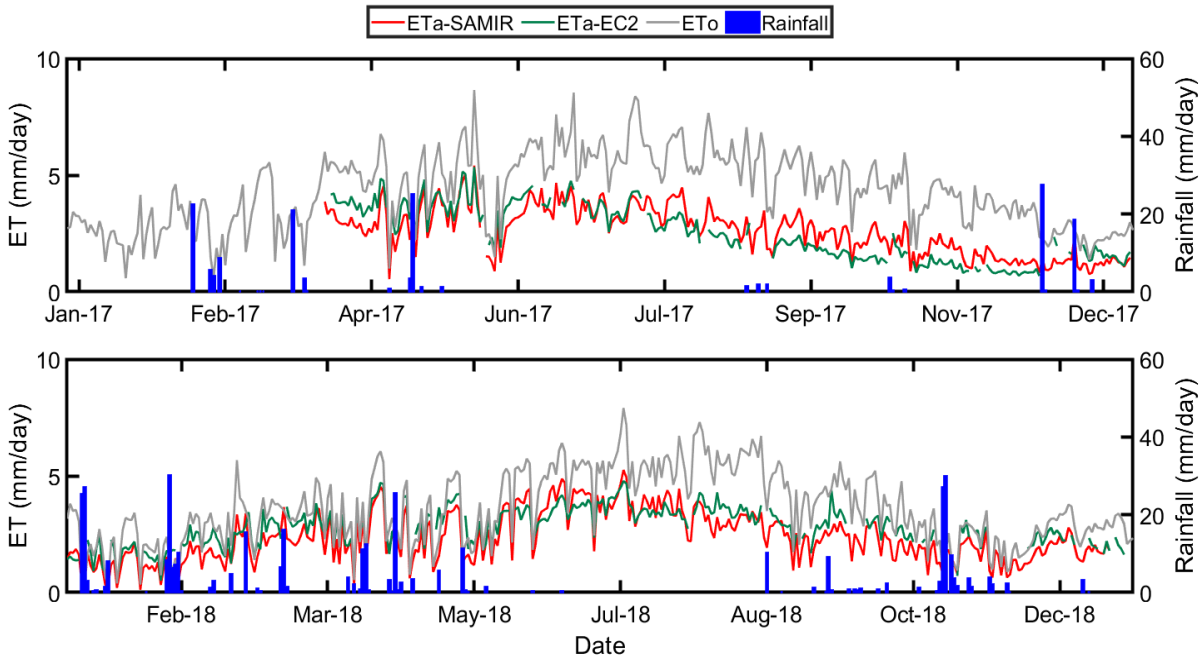

Figure 6: ETa measured by EC2 and estimated over the EC2 footprint by SAMIR during the study period 2017 and 2018.

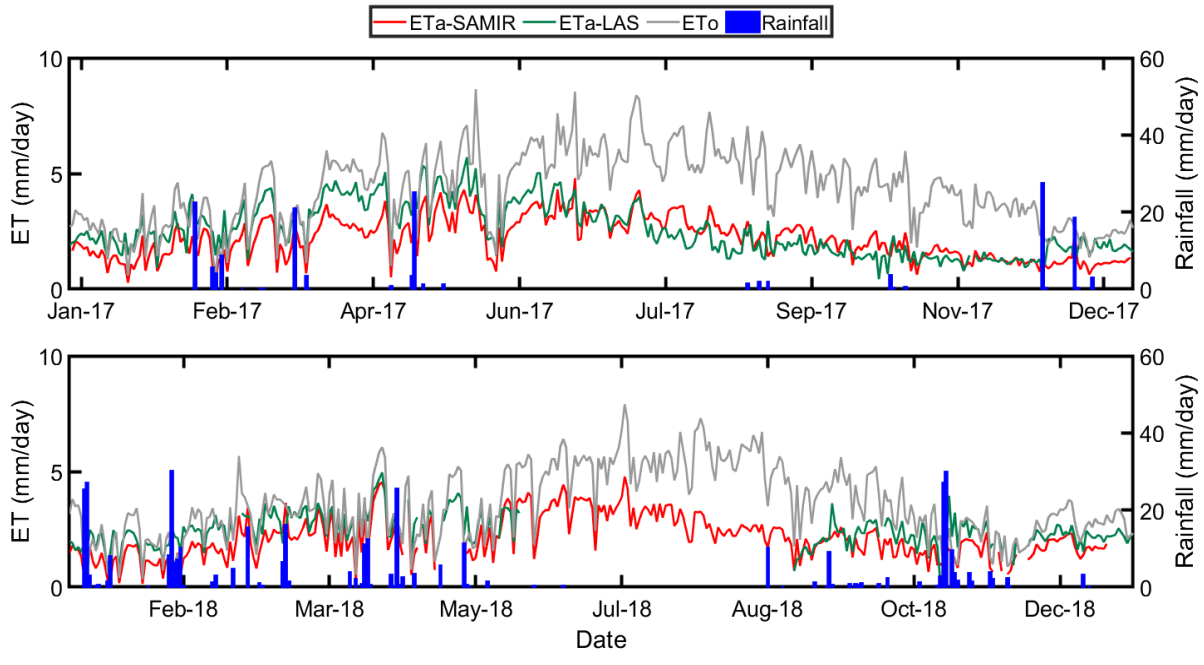

Figure 7: ETa measured by LAS and estimated over the LAS footprint by SAMIR during the study period 2017 and 2018.

3.3 SPARSE calibration

As for SAMIR, the SPARSE model was calibrated over the EC1 station, by minimizing the RMSE between simulated and observed LE. The SPARSE results were weighted by the EC and LAS instantaneous footprints at the time of Landsat overpass. From a sensitivity study (Boulet et al., 2015), five parameters of SPARSE having a significant impact on simulated ETa were calibrated : the minimum stomatal resistance (rst_{min}) which was set to 260 s/m, As reported by Zhu et al. (2014) rst_{min} varies for many natural and cultivated plants it ranges considerably from 20 to 100 s/m for crops and from 200 to 300 s/m for many types of trees (Zhu et al., 2014). Leaf width (w) set to 0.03 m is within the range found in the literature (Saadi et al., 2018; Ait Hssaine et al., 2018; Braud et al., 1995). The ratio relating the net radiation of the soil to the heat soil flux (ξ) set to 0.13. In fact, Kustas et al. (1993) pointed that ξ is driven by several factors namely the time of day, the soil moisture and the thermal properties, as well as the vegetation density and its value ranges between 0.05 and 0.5. The extinction coefficient (k) in the equation where the fraction cover is calculated in term of LAI which is set to 0.6 which is in conformity with the values found by Connor et al. (2012) and Srinet et al. (2019). The empirical coefficient in the aerodynamic resistance (n_{SW}) set to 2.5 which is the same value stated by Boulet et al. (2015). The calibration shows an acceptable agreement with an RMSE and R of about 81.3 W/m^2 and 0.58, respectively (Figure 8).

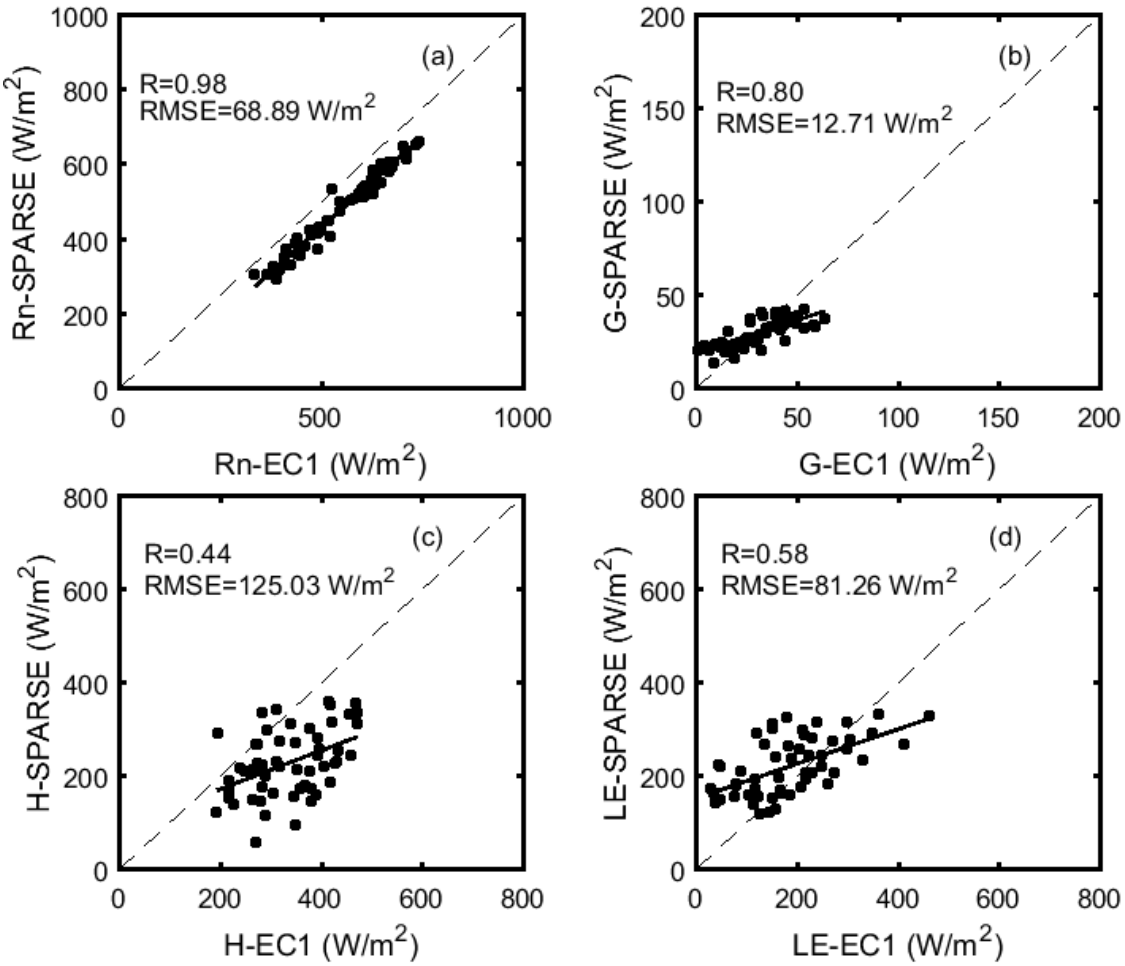

Figure 8: Comparison between the EC1 measurements and SPARSE estimations (Net radiation (Rn), soil heat flux (G), sensible heat flux (H) and latent heat flux (LE)) using Landsat products.

3.4 SPARSE validation

The parameters obtained over EC1 were validated locally over EC2 and spatially using the LAS measurements. Scatter plots of modeled available energy, sensible and latent heat fluxes for Landsat overpass dates, averaged over the EC2 and LAS footprints versus measurements are displayed at figures 9 and 10. Net radiation values were accurately estimated by SPARSE with RMSE of about 69.8 W/m^2 for EC2. However, they show an underestimation compared to the two stations measurements which is expected since the Landsat LST overestimates the surface temperature as shown in figure 2. This is in-line with the same bias observed in the calibration phase. Rn measurement over a complex surface is a difficult task as many authors reported (Anthoni et al., 2000; Byun et al., 2014) due to the influence of the vegetation structure on the albedo. Comparison between observed and simulated soil heat flux shows lower agreement than for Rn which can be explained in one hand by the accuracy of the measurements since it gathers several difficulties as reported in the literature (Ezzahar et al., 2009b; Ait Hssaine et al., 2018). These difficulties lay in the plate protection from direct sunlight especially for the one at 5 cm and choosing the representative position which takes into consideration the vegetation intercept of the

388 incoming radiation. On the other hand, SPARSE calculates G as a fraction of Rns inducing the
389 transmission of the error on Rns to G. Furthermore, for ease of implementation, a constant fraction value
390 was adopted in this study, whereas many studies have related the value of this fraction to the variation
391 of the surface cover (Diarra et al., 2017; Kustas, 1990; Saadi et al., 2018). Sensible heat flux simulations
392 show acceptable agreement over EC2 and LAS with an RMSE of about 116 W/m^2 and 68 W/m^2,
393 respectively. The discrepancy showed in the figures between modeled and observed H can be attributed
394 to numerous factors, particularly the accuracy of LST data. In addition, the calculation errors on the
395 surface resistances are strongly affecting the H estimation. Also, one potential source of error is the
396 accuracy of the displacement height (d) and roughness length (Z_0) which were estimated in this work as
397 a fraction of the vegetation height using the rule of thumb (Z_0 = 0.14*hveg and d = 0.66*hveg, hveg is
398 the vegetation height) following Brutsaert and Kustas (1987). The method used to approximate these
399 parameters are adapted to dense and homogeneous areas whereas the experimental field is
400 heterogeneous and sparse. Finally, the model provides good estimates of LE over EC2 and LAS with an
401 RMSE of about 52.7 W/m^2 and 78.8 W/m^2, respectively. The discrepancy in LE can be related to the
402 uncertainty on H and AE $(Rn - G)$ which is directly transmitted to LE values since it's a residual term
403 of the energy balance (Kalma et al., 2008; Morillas et al., 2013; Saadi et al., 2018). Moreover, using
404 constant parameters during the whole year despite vegetation and environmental changes can causes
405 some errors, especially for the minimum stomatal resistance (rst_{min}). As reported by Boulet et al.
406 (2015) an inadequate value of rst_{min} increases automatically H and LE errors.

407

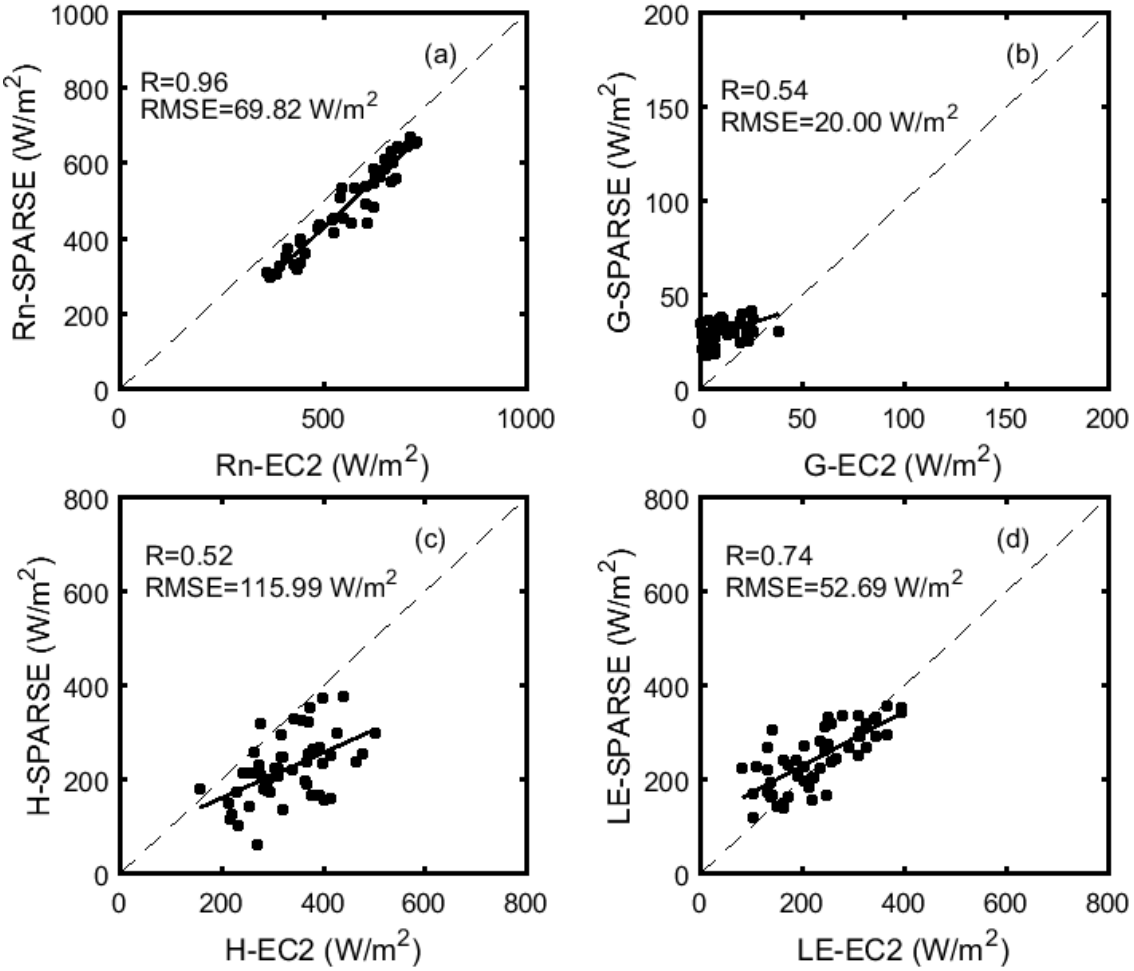

408

409 *Figure 9: Same as figure 8 but for EC2.*

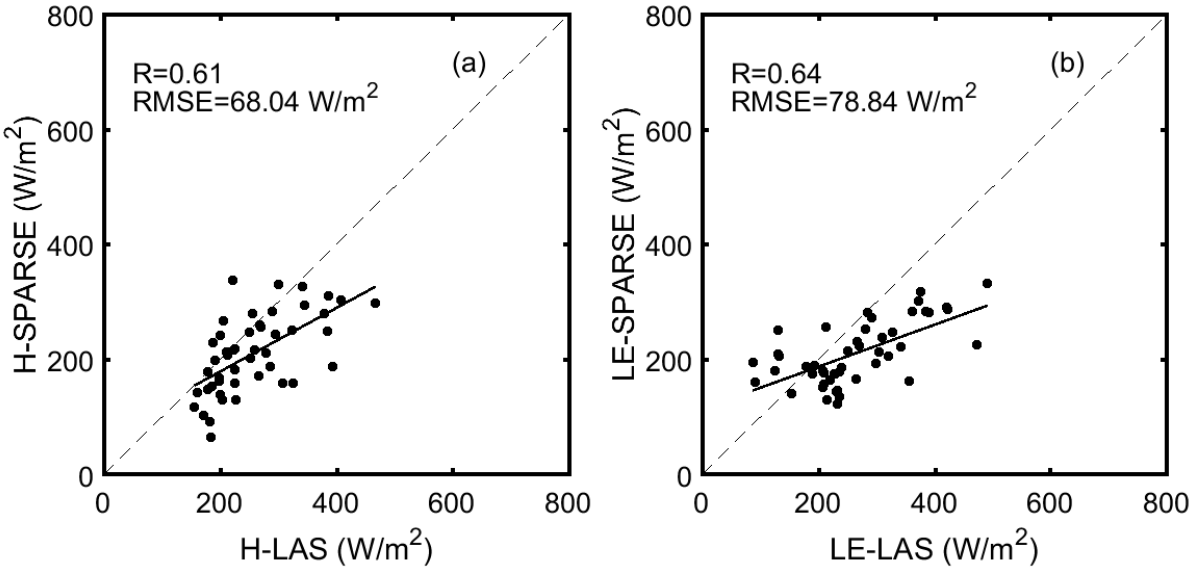

410

411 *Figure 10: Comparison between the LAS measurements and SPARSE estimations* (*H and LE*) using *Landsat products.*

3.5 Model's validation and intercomparison

The comparison of the four models and LAS and EC2 measurements was done at the daily scale. The instantaneous ETa estimates provided by SPARSE and SW were extrapolated to a daily value using the EF method presented in section 2.5. Then, daily ETa maps provided by all models were weighted using the daily footprint of the LAS and EC2 measurements in order to be compared with them.

Figure 11 and 12 presents the scatterplots of the four models ETa estimates compared to the EC2 and LAS measurements, respectively. The four models underestimate the LAS measurements which is strange and raises the question on the LAS accuracy. However, the LAS values were validated while comparing them with the EC1 and EC2 values in a previous study (Elfarkh et al., 2020) and the results were good. SPARSE and SW are more scattered which can be related to the large number of their parameters that are taken constant throughout the season. Nevertheless, these parameters are variable in space depending on the soil and vegetation characteristics. In addition, the sensibility of both models to the LST data errors can also generate this bias. The METRIC and SAMIR ETa estimates are less scattered and show better statistical results compared to SPARSE and to SW. The time series of the daily ETa values obtained with the LAS and the four models are illustrated in figure 13. Overall, the LAS and the four models ETa show similar seasonal dynamics. They increase with the begin of the growing season in January, reach maximum values during growth peak in April-May, and then decrease until December. Since precipitation and canopy development greatly affect ET, its rates decrease during dry conditions and increase immediately after each rainfall event. The ETa values of winter are higher in 2018 than in 2017 due to the higher precipitations in 2018. However, the ETa spring values are low in 2018 compared to 2017, which can be attributed to the low available energy received due to more frequent cloudy days.

During summer 2017, SW was close to the LAS measurements. SPARSE underestimates ETa values, which may be due to the already observed overestimation of Landsat LST (Figure 2) that signify stress conditions for the model. In contrast, the effect of the LST error on the SW estimations was not as strong as for SPARSE, which can be attributed to fact that the absolute values of LST are used in SPARSE, whereas LST was used in a relative manner in SW model to compute stress indexes related to the resistances of vegetation and soil. Regarding SAMIR, the estimated ETa values were overestimated which is expected since SAMIR doesn't stop irrigation in summer despite the water shortage. METRIC in this period shows a slight overestimation that can be linked to wet edge detection error under these stress conditions. The RMSE and the R of the models show that SAMIR and METRIC-GEE are the least scattered and the most correlated to the measurements. On the other hand, SPARSE shows less bias and dispersion than SW while the latter is better correlated.

In order to further compare the models and illustrate the discrepancies, ETa images of the four models are shown for three dates illustrating contrasted conditions (Figure 14). The accuracy of each image is

assessed through the bias with the LAS measurements (Figure 15); keeping in mind that the LAS measurements represent only the irrigated area in the center of the image. For the 16th of January 2017, the model providing the best estimates is SPARSE, and the other models strongly underestimate ETa (-1.5 to -1 mm bias). SAMIR shows low values of ET, especially over the bare soil supposedly not irrigated and also over the wheat plots which were bare soil at this time (Figure 14). SW model also underestimates ETa which can be explained by the non-representativeness of the relation established between the stress indexes and the resistances over the bare soil since these relations were calibrated over olive trees (EC1). In contrast, thanks to the thermal information which is highly correlated to the soil moisture, SPARSE shows less bias compared to the LAS. Finally, METRIC-GEE underestimates the most ETa although it is based on thermal remote sensing that should capture soil moisture conditions. Indeed, the METRIC approach forces the flux computation to be bounded between wet and dry extreme conditions, although these extreme conditions are not always present on every image and may thus induce a wrong scaling. For the summer date of 20 august 2017, SW and SAMIR models provide the best results. METRIC-GEE shows the higher bias which can be explained by the error on determining the wet and dry temperatures which are not well identified in such dry uniform conditions. SPARSE also underestimates ETa measurements which may be related to the LST reliability. On first April 2018, during the development stage of annuals and no stress conditions, SAMIR model is close to the LAS observations, whereas SW shows a strong underestimation. The SW and SPARSE underestimation can be explained by the fact that several parameters, especially the minimal stomatal conductance, are set constant during the entire season regardless of the seasonal changes. This assumption can lead to erroneous ETa estimates. In fact, Zhu et al., (2013) and Hu et al., (2009) noted that over/underestimation of ETa can occur when using constant parameters for long-term simulations using SW over different vegetation and environmental conditions. Finally, for METRIC-GEE, we observe a strong contrast between vegetation area with very high ETa and bare soil areas with low ET, which is a characteristic of METRIC always stretching ETa between dry bare soil and wet vegetated areas (Tasumi, 2019). However, despite a strong ETa in vegetated areas, the model predictions are still underestimated at the scale of the LAS footprint, due to the underestimation of evaporation in the riverbeds (see below).

Another difference between the models is linked to riverbed. SAMIR shows low ETa for all dates in the river, assuming a non-irrigated bare soil, without taking into consideration the evaporation due to capillary rise from the shallow aquifer associated with riverbeds. This is well visible on the April image and to a lesser extent in January, in contrast, SPARSE accounts for the soil moisture related to surface temperature and shows higher ETa in riverbeds for these two dates. Although based on thermal data, SW also underestimates ETa in this area, which is explained by the fact that the resistance calibrations were done mainly on olive trees (EC1). This calibration may not be representative of the entire study area, in particular the fields of annual crops. Calibration of the resistance's equation in the SW model on different land uses is necessary to improve its performance.

On the whole, the accuracy of the four approaches for predicting ETa was acceptable despite some discrepancies observed in specific conditions but not at the same time depending on the model. There is no unique method for evaluating models, so there is no easy answer to the question of which model is most accurate. It seems that the SPARSE model, like other models based on thermal remote sensing, even if it is based on physical assumptions, remains sensitive to the quality of the input variables on one hand (e.g. the accuracy of the surface temperature), and on the other hand to the setting of the different physical parameters required by the model. The latter parameters are very variable in space and their calibration may suffer from equifinality problems as shown by the calibration of SPARSE. The errors of the three energy balance models, SPARSE, SW and METRIC-GEE seem uncorrelated which lead to a logical hypothesis of testing the potential benefit of computing their average value. As shown in figure 16, the correlation coefficient obtained between this average ETa value and the measurements shows an improvement of 36%, 29% and 3% as compared to SPARSE, SW and METRIC-GEE, respectively. However, this average is underestimated with a bias of about -0.63 mm/day which is expected since the three model estimations are underestimated. Given that the bias can be corrected based on the linear relation obtained, the improvement in the correlation between ETa values average and the LAS measurements may be exploited for operational ETa estimates in this area. This approach of averaging different methods is a technique that has been used in different works such as the EVASPA model that includes several algorithms for calculating ETa in order to assess the uncertainties in ETa estimates. (Gallego-Elvira et al., 2013).

In comparison with thermal approaches, SAMIR provides a good ETa because it is computed on a robust base which is the slowly changing NDVI and accurately measured ET_0, however it suffers from a major drawback which is the lack of control of soil water conditions. Thus, water stress affecting both transpiration (K_s) and evaporation (K_e) is poorly represented. Models do not have the same advantages and weaknesses and each may be suitable under certain conditions (Table 3). The major constraint is the need of user calibration each time the environmental conditions are different except for METRIC-GEE for which there are achieved automatically. In addition, the availability of the model's input is a paramount element to choose a model especially in traditional complex areas. For instance, it is impossible to have spatial information about the irrigation of each plot. Consequently, SAMIR is not the best choice in stress conditions where soil moisture strongly influences ET. On the other hand, the difficulty to calculate accurate LST from the satellite's thermal bands is an issue for the energy balance models due to their high sensitivity to this variable. However, these models are not equally affected by LST accuracy. SPARSE is highly sensitive to LST accuracy since the error directly impacts H and LE. In contrast, the contextual approach of METRIC-GEE "scaling" LST relatively to extreme values of the image reduces problems. Also, for SW, the relative variation of LST between its maximum and minimum is used to calculate the soil and the vegetation resistances. This means that the error on LST will not have the same effect on METRIC-GEE and SW as compared to SPARSE. One advantage of

SAMIR is to produce continuous daily ETa estimates which is valuable in assessing the basin water budget (Simonneaux et al., 2007; Le Page et al., 2012; Diarra et al., 2017). SPARSE is a model that can be used accurately to detect stress conditions if properly calibrated (Boulet et al., 2015). Consequently, ETa estimated by SPARSE can be used to calculate stress indices. The modified SW model is a new approach that must be tested under different conditions in order to find a robust relationship that accurately represents the variation in resistance as a function of stress indices. Finally, METRIC-GEE showed a good agreement with the LAS measurements, which is very good news since it is available freely and it does not require in-depth technical knowledge.

Table 3: Summary table of the advantages and disadvantages for the four models.

Models	Disadvantages	Advantages
SPARSE	- Very sensitive to LST accuracy - Many physical parameters required - Need of calibration - Extrapolation instantaneous ETa to daily values add errors	- Few inputs needed - Reliable in stress condition
SAMIR	- Irrigations are necessary and are estimated - Need of calibration (especially for the soil evaporation component)	- Provide continuous daily ETa values - It can provide accurate ETa values in no or limited stress conditions.
SW	- It is a new approach that need calibration / validation on other sites	- Few inputs needed
METRIC-GEE	- Sensitive to the error in the dry/wet edges detection - You cannot download large zone from the platform	- No calibration needed - Available to download freely - Ease of access. No need for in-depth technical knowledge

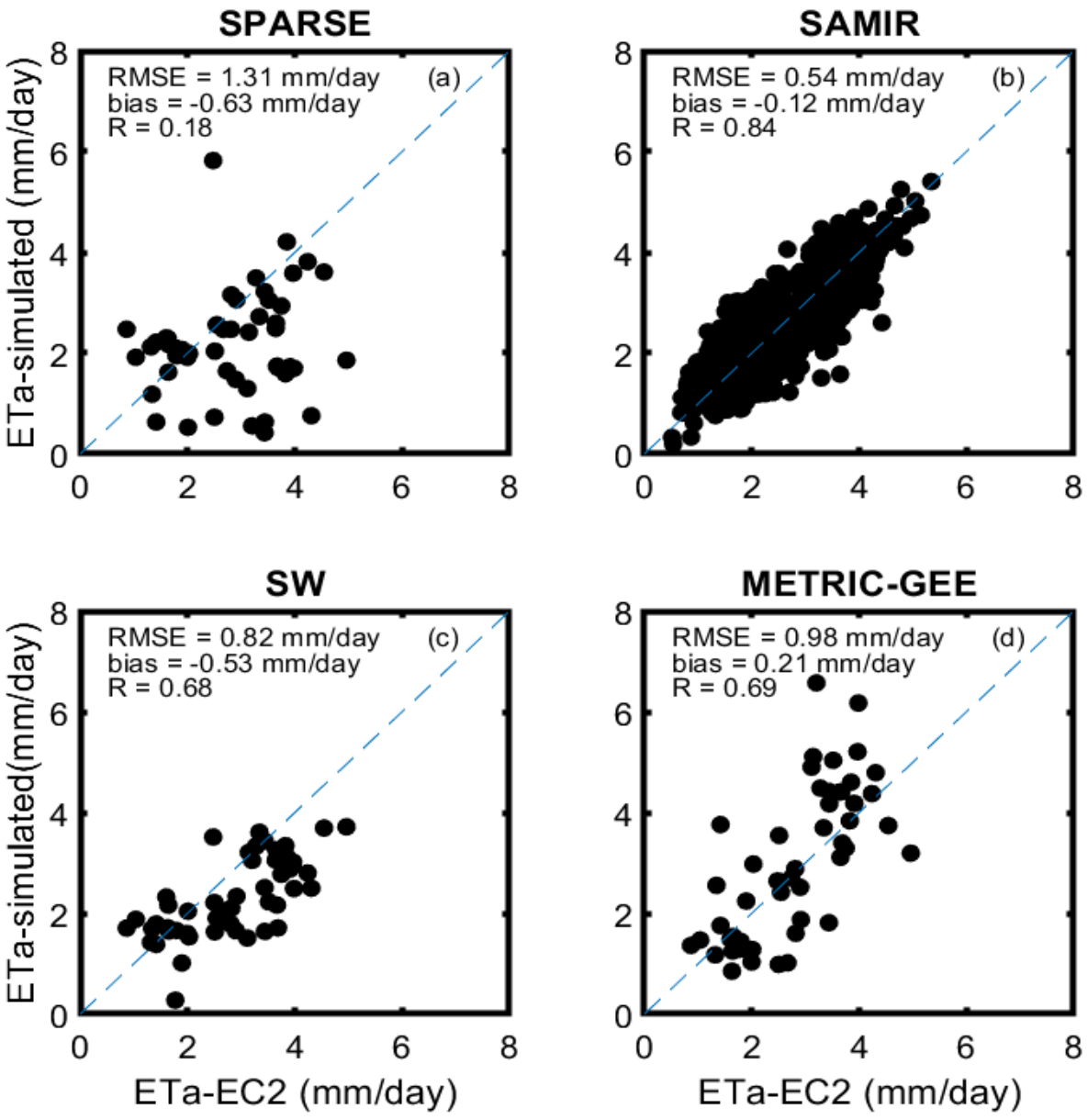

529

530 *Figure 11: Comparison between ETa measured by EC2 and estimated by SPARSE (a), SAMIR (b), SW (c) and METRIC-GEE (d).*

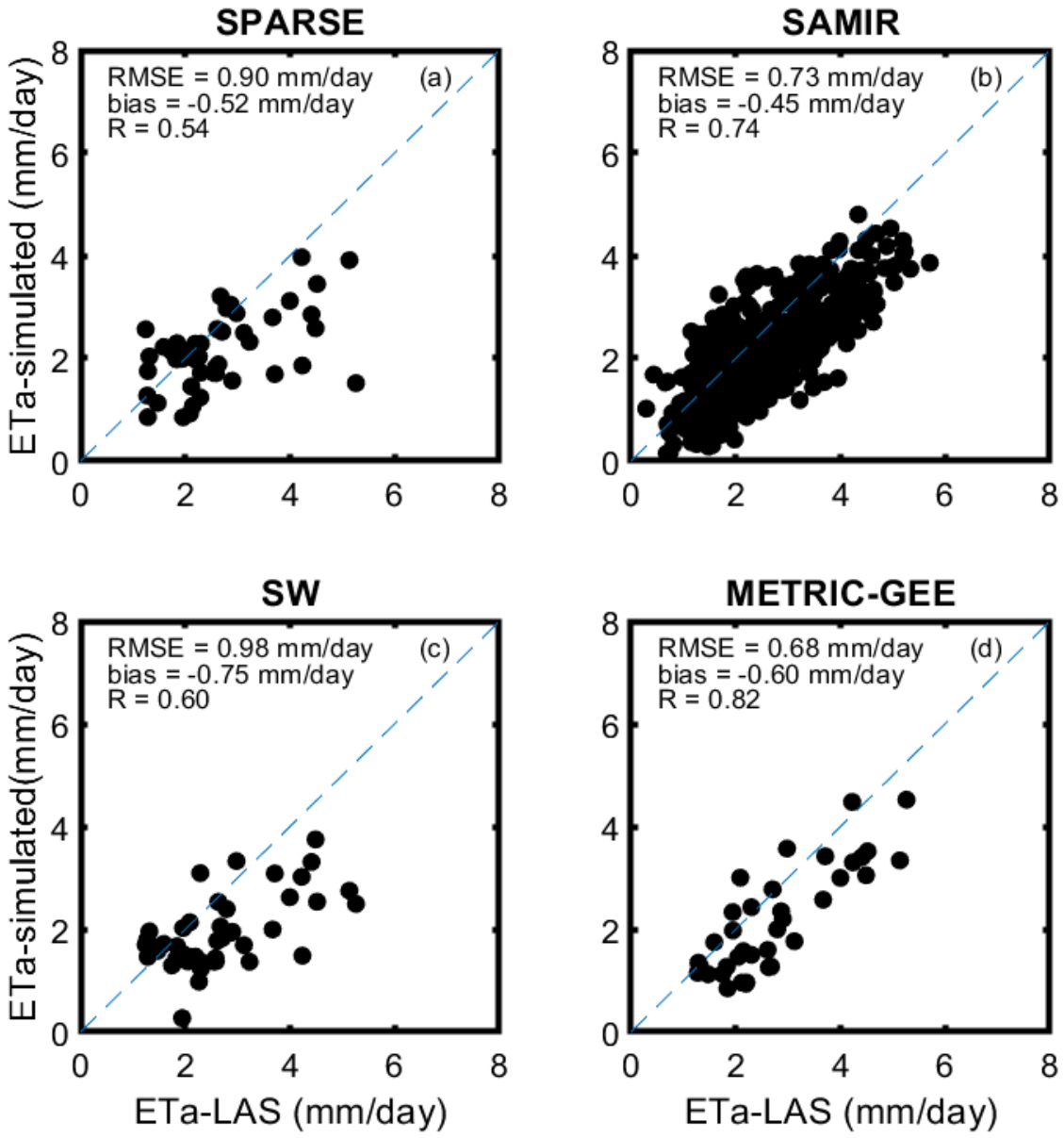

531

532 *Figure 12: Comparison between actual ETa measured by the LAS and estimated by SPARSE (a), SAMIR (b), SW (c) and*
533 *METRIC-GEE (d).*

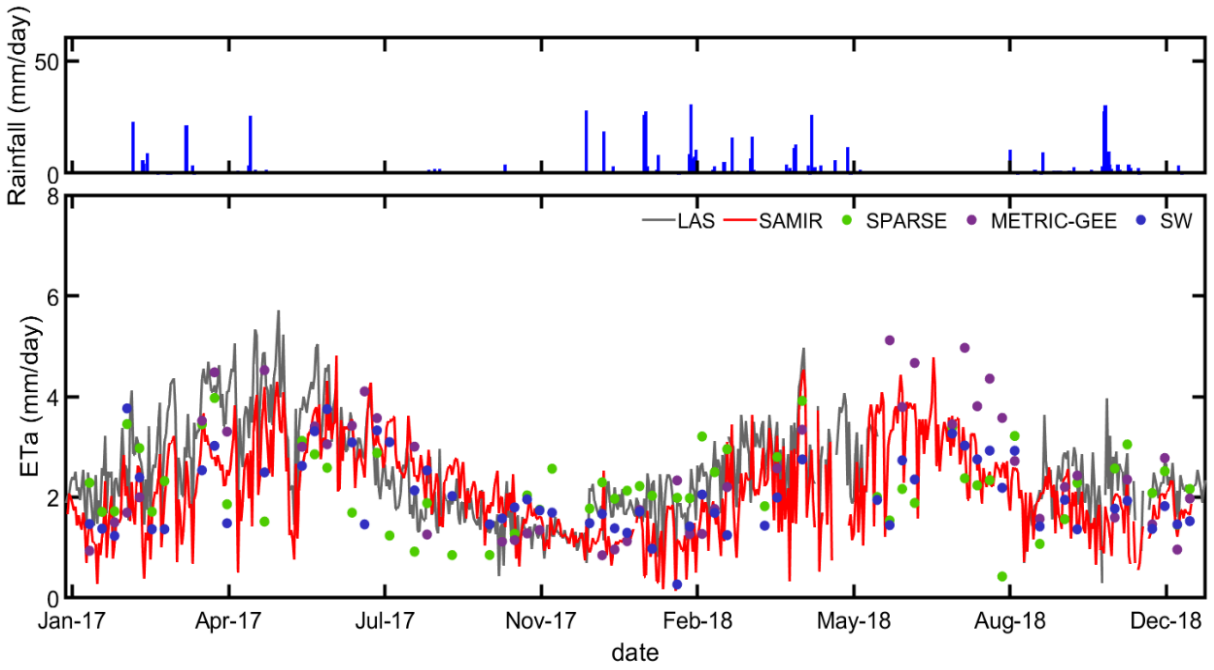

534

535 *Figure 13: Daily series of the rainfall, ETa measured by LAS and estimated over the LAS footprint by SAMIR, SPARSE, SW and*
536 *by METRIC-GEE during the study period 2017 and 2018.*

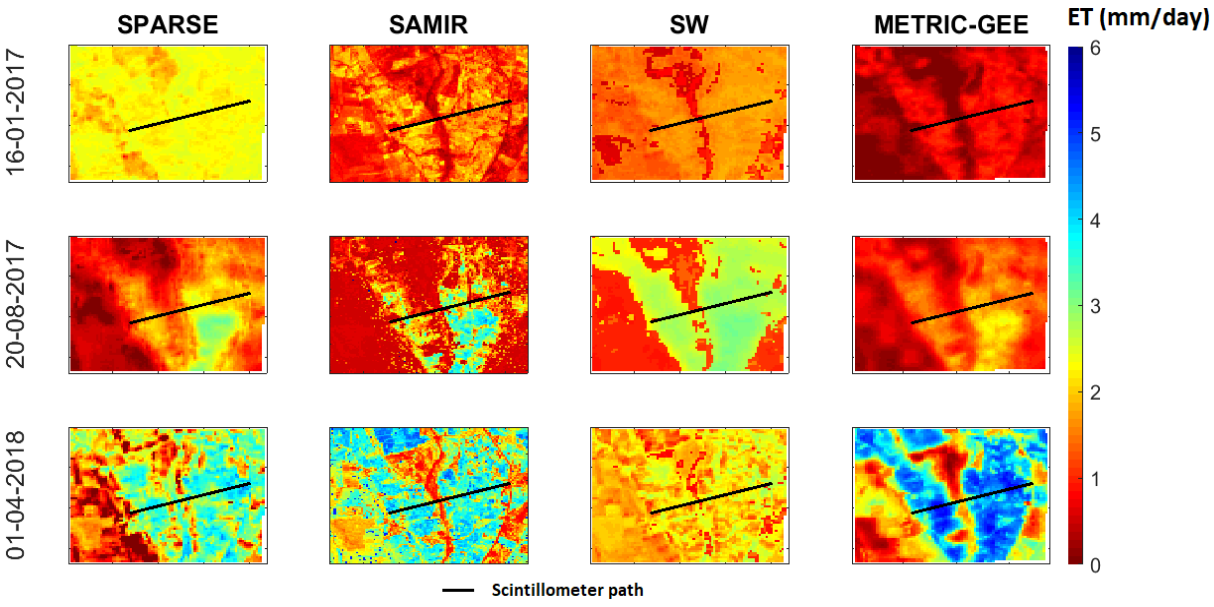

537

538 *Figure 14: ETa maps for three days of contrasting climate conditions estimated by SPARSE, SAMIR, SW and METRIC-GEE.*
539 *SAMIR outputs have a 10 m spatial resolution whereas the other models' outputs have a 30 m pixel)*

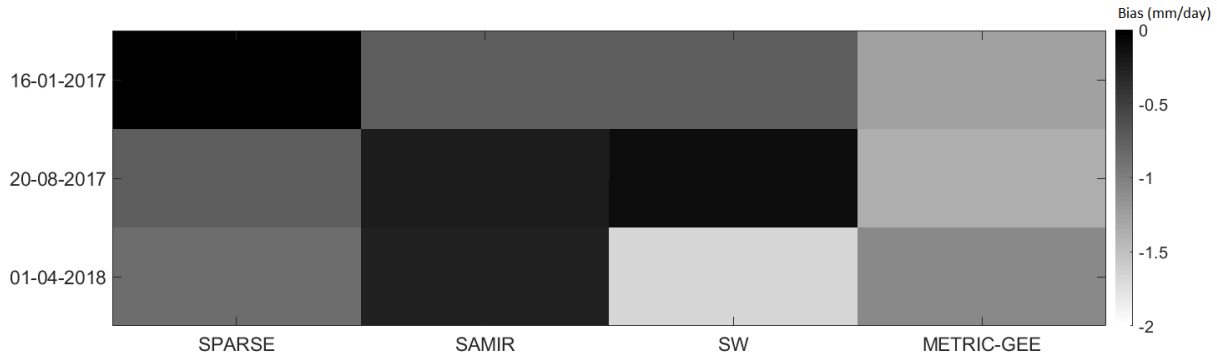

Figure 15: Bias in mm/day between the model maps shown in Figure 13 and LAS measurements.

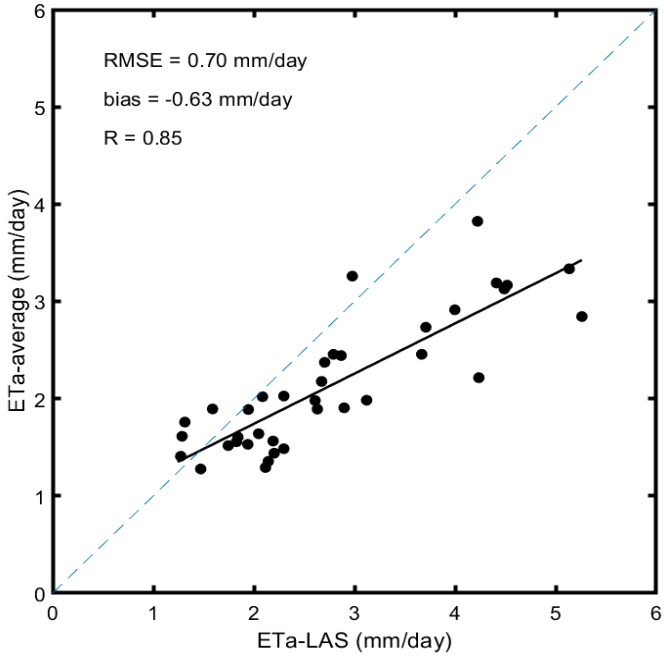

Figure 16: Comparison between the ETa measured by the LAS and the average of SPARSE, SW and METRIC-GEE ETa estimation.

4 Conclusion

The objective of this study was to map distributed actual crop evapotranspiration (ETa) at high resolution using different approaches based on different remote sensing data. We used the SAMIR model based on water budget as proposed by the FAO-56 approach, and three approaches based on thermal remote sensing, namely the SPARSE model, a modified version of Shuttleworth-Wallace (SW) model and an operational version of METRIC available on Google Earth Engine (METRIC-GEE). The comparison has been performed over an heterogeneous and complex irrigated agricultural area. Landsat 7 and 8 products were used for SPARSE, SW and METRIC-GEE and Sentinel 2 products were used for SAMIR. The models' performance is evaluated using two Eddy covariance (EC) systems and scintillometer (LAS) measurements. The seasonal variability of ETa is correctly predicted by the four models throughout 2017 and 2018 agricultural seasons. However, SAMIR and METRIC-GEE, with an

RMSE of 0.73 and 0.68 mm/day respectively as compared to LAS measurements showed slightly better performances in estimating ETa than SPARSE and SW which show an RMSE of 0.90 and 0.98 mm/day compared to LAS measurements, respectively. Finally, when averaging the estimates of the three thermal based models, the correlation coefficient with measurements was improved by 36%, 29% and 3% compared to SPARSE, SW and METRIC-GEE, respectively.

This study has shown the accuracy of different approaches and highlights the importance of remote sensing data which allow highly spatial and temporal resolution of ETa estimation. SAMIR has represented good estimation of ETa but its dependence for water input data (irrigation and rainfall) limit its applicability especially over traditional irrigated areas. On the other hand, thermal approaches may detect water stress but they have shown to be very sensitive to parameterization and to uncertainties in input data. This is the case for the remotely sensed surface temperature and for parameters like the stomatal resistance, sensitive to environmental conditions. Interestingly enough, METRIC-GEE ETa products showed good agreement with the LAS measurements without any calibration and are freely available online. These results confirm the idea that to move forward, the combination of these models can be applied. For instance, assimilating the ETa estimates of METRIC-GEE, SW or SPARSE into SAMIR which showed a good temporal consistency but whose widespread application may be limited by lack of available, spatially-explicit data on irrigation amount. This potential synergy is expected to be improved in the next few years with the LSTM mission of ESA and the TRISHNA mission (Lagouarde et al., 2018) which will provide high spatial-temporal resolution land-surface temperature at a resolution of 50 m, every 3 days, which is a significant step forward as compared to the actual Landsat data (100 m, every 16 days). This will allow accurate monitoring of spatio-temporal changes in the water status of surfaces, including crop stress detection, and will open great opportunities to improve these models to be more adapted for assessing crops water demand at field scale.

Acknowledgments

This research was conducted within the Joint International Laboratory TREMA (https://lmi-trema.ma). Setup was funded by CNRST SAGESSE project and German Cooperation Giz within the frame of the Hydraulic Basin Agency of the Tensift (ABHT). The authors wish to thank the projects: RISE-H2020-ACCWA (grant agreement no: 823965), PHC TBK/18/61, PRIMA-IDEWA, PRIMA-ALTOS and ERANETMED03-62 CHAAMS for partly funding the experiments.

Appendix 1: SAMIR model

SAMIR, is a tool to compute ETa and water budget at the daily time step using the FAO method (Allen et al., 1998). The soil model has been slightly modified to include three compartments, namely the evaporation, root and deep soil compartments (Saadi et al., 2015). Between these compartments, water can move down by gravity or up and down by diffusion processes. These fluxes are linked to the soil moisture of the compartments. In this work, FAO dual crop approach implemented in the SAMIR tool was used to calculate ETa as follows:

$$ETa = (K_s K_{cb} + K_e) ET_0 \quad \text{Eq: A.1}$$

The reference evapotranspiration (ET_0) was calculated using meteorological measurements based on the FAO Penman-Monteith equation and the crop coefficient K_{cb} was estimated using a $NDVI - K_{cb}$ relationship based on satellite time series imagery:

$$K_{cb} = a * NDVI + b \quad \text{Eq: A.2}$$

Parameters a and b are related mainly to land cover type and climatic conditions and can be calibrated or/and taken from previous studies (Duchemin et al., 2006; Er-Raki et al., 2007; Saadi et al., 2015).

K_e is the evaporation coefficient. When the depletion in the evaporation layer (i.e., void volume, De) exceeds a threshold (i.e., readily evaporable water, REW), a reduction factor K_r is applied to reduce evaporation following Eq. A.4.

$$K_e = min(K_r(Kc_{max} - K_{cb}), f_{ew}.Kc_{max}) \quad \text{Eq: A.3}$$

$$K_r = m\frac{TEW - De}{TEW - REW} \leq 1 \quad \text{Eq: A.4}$$

where Kc_{max} and f_{ew} are the maximum capacity of water evacuation by atmosphere and the fraction of soil wetted, respectively. TEW is the total evaporable water in the evaporation layer. In order to estimate Kr, we used the formalism proposed by (Torres & Calera, 2010), namely the introduction of the m parameter which allows more reduction of evaporation as compared to the original FAO-56 formalism. The m coefficient initially set to 1 allows to further reduce the evaporation level with m values potentially decreasing until 0. This choice was made because, like Torres et al., we observed a strong overestimation of ETa especially after wetting events which was supposed to be due to higher evaporation (Saadi et al. 2015). After introducing the m parameter and calibration, better estimates of ETa were obtained (Saadi et al., 2015). The combination of REW and m are functionally defining the surface resistance to the soil evaporation.

The stress coefficient K_S is computed when depletion in the root compartment (Dr) is higher than the readily available water (RAW), limiting the root uptake (Eq. A.5). RAW is a fraction of the TAW, the total available water available for vegetation.

$$K_S = \frac{TAW - Dr}{TAW - RAW} \leq 1 \qquad \text{Eq: A.5}$$

In addition to NDVI time series, SAMIR uses as forcing the daily reference evapotranspiration (ET_0) values and water input. In fact, rainfall can be measured using the meteorological station, whereas irrigation cannot be easily observed for each plot in an area. Thus, SAMIR simulated the water inputs based on an assumed behavior of the farmer, regarding the threshold in soil moisture to trigger irrigation, and the water depth brought. A detailed explanation of SAMIR functioning may be found in (Saadi et al., 2015).

Some parameters were fixed according to the guideline of the FAO-56 paper (the depth of the soil evaporation layer (Ze), the root zone water depletion fraction before stress (p) and the maximum value of crop coefficient (following rain or irrigation) which is determined by the energy available for ETa at the soil surface (Kc_{max})), or were based on ground data (the volumetric water content at field capacity (ω_{fc}) and the volumetric water content at wilting point (ω_{wp})). Vegetation fraction cover values were computed based on a linear relationship with NDVI where the slope (a_{fc}) and the intercept (b_{fc}) were set assuming an NDVI value for the bare soil ($fc = 0$) and full coverage ($fc = 1$) equal to 0.15 and 0.9, respectively. fc was used to calculate the root zone depth (Zr) using a linear relation and assuming that the crop will reach its full rooting depth at maximum fc. The remaining parameters (the slope and the intercept of the NDVI-K_{cb} linear relationship (a_{Kcb} and b_{Kcb}), the readily evaporable water (REW), the root depth (Zr_{max}) and the diffusion between surface and root layers (Dif_{er})) were calibrated using the flux data (Table 2).

Appendix 2: SPARSE model

The SPARSE model is a two-source model solving separately the energy budget of the soil and the vegetation (Boulet et al., 2015), where both of them are connected to the atmosphere separately. The model solves a system of equations regarding sensible and latent heat flux for soil and vegetation respectively (Eq. A.6 and A.7) and the energy balance of the soil and the vegetation (Eq. A.8 and A.9). Eq. A.10 describes the link between the average surface temperature and longwave radiative fluxes.

$$H = H_S + H_V \qquad \text{Eq: A.6}$$

$$LE = LE_S + LE_V \qquad \text{Eq: A.7}$$

$$Rn_S = G + H_S + LE_S \quad \text{Eq: A.8}$$

$$Rn_V = H_V + LE_V \quad \text{Eq: A.9}$$

$$\sigma \varepsilon LST^4 = \varepsilon R_{atm} - R_{an} \quad \text{Eq: A.10}$$

H is the sensible heat flux, LE is the latent heat flux, Rn is the net radiation and G is the soil heat flux; indexes "s" and "v" are for the soil and the vegetation, respectively. ε is the surface emissivity. R_{atm} is the incoming atmospheric longwave radiation, R_{an} is the net longwave radiation, LST is the radiative surface temperature (K) and σ is the Stefan-Boltzmann constant. To solve these equations, the model is first run in prescribed mode for two extreme configurations, namely fully unstressed and fully stressed vegetation (i.e. for a minimum and a maximum surface resistances), computing theoretical evaporation and transpiration fluxes based on the same method as the TSEB model (Kustas & Norman, 1999). These potential fluxes are then used as thresholds in the retrieval mode. In this mode, LE_V is calculated first considering unstressed conditions, deducting LE_S using the measured surface temperature. If the obtained LE_S value is negative, the unstressed vegetation assumption is invalid. In that case, the vegetation is assumed to suffer from water stress and the soil surface is assumed to be dry. Consequently, LE_S is set to 30 W/m^2 to account for the remaining slow vapor diffusion within the soil (Boulet et al., 1997) and the vegetation latent heat flux (LE_V) is recalculated. If LE_V is also negative, both LE_S and LE_V components are given zero independently of LST.

Appendix 3: Shuttleworth–Wallace model

This model is developed by Shuttleworth and Wallace in 1985 (Shuttleworth & Wallace, 1985). It estimates two separate fluxes one for soil and the other for the vegetation using the following formulas:

$$ETa = E + T = C_s PM_s + C_v PM_v \quad \text{Eq: A.11}$$

$$PM_s = \frac{\Delta A + \left[\left(\rho C_p D - \Delta r_a^s (A - A_s)\right)/(r_a + r_a^s)\right]}{\Delta + \gamma[1 + r_s^s/(r_a + r_a^s)]} \quad \text{Eq: A.12}$$

$$PM_v = \frac{\Delta A + \left[\left(\rho C_p D - \Delta r_a^v A_s\right)/(r_a + r_a^v)\right]}{\Delta + \gamma[1 + r_s^v/(r_a + r_a^v)]} \quad \text{Eq: A.13}$$

where A_s and A are available energy above soil surfaces and canopy (W/m^2), respectively. Δ is the slope of saturation vapour pressure curve (kPa/K), ρ is the air density (kg/m^3), C_p is the specific heat of dry air at constant pressure (J/kg/K), D is the water vapor deficit (kPa), γ is the psychrometric constant (Pa/K).

In this study a modified version of SW model is used. This version used the thermal data to provide spatial ETa estimation as described by Elfarkh et al., (2021). In this approach the vegetation and soil resistances were related to the stress indexes as follow:

$$r_s^s = ae^{b*SI_{ss}} \quad \text{Eq: A.14}$$

$$r_s^v = ce^{d*SI_{sv}} \quad \text{Eq: A.15}$$

where a, c, b and d are the calibration parameters set to 160.25 and 36.02 s/m, 2.62 and 1.30, respectively. r_s^s and r_s^v are the resistances for soil and for vegetation, respectively. SI_{ss} and SI_{sv} are the stress indexes for soil and vegetation, respectively. This approach was calibrated and validated in the same study area (Elfarkh et al., 2021).

Appendix 4: METRIC-GEE model

METRIC-GEE is a version of METRIC (Allen et al., 2007) that operates on the Google Earth Engine system (https://eeflux-level1.appspot.com/). The surface energy balance in this model is derived by Landsat thermal band while the surface roughness, vegetation amounts and albedo are retrieved from short-wave bands. The instantaneous evaporative fraction estimated at the time of satellite overpass is extrapolated at daily scale to provide daily ETa value using reference ET computed by the Penman-Monteith and GridMET weather data sets.

References

Allen, R. G., Pereira, L. S., Howell, T. A., & Jensen, M. E. (2011). Evapotranspiration information reporting: I. Factors governing measurement accuracy. *Agricultural Water Management*, *98*(6), 899–920. https://doi.org/10.1016/j.agwat.2010.12.015

Allen, R. G., Pereira, L. S., Raes, D., & Smith, M. (1998). Crop evapotranspiration: Guidelines for computing crop requirements. *Irrigation and Drainage Paper No. 56, FAO*. https://doi.org/10.1016/j.eja.2010.12.001

Allen, R. G., Tasumi, M., & Trezza, R. (2007). Satellite-based energy balance for mapping evapotranspiration with internalized calibration (METRIC) - Model. *Journal of Irrigation and Drainage Engineering*, *133*(4), 380–394. https://doi.org/10.1061/(ASCE)0733-9437(2007)133:4(380)

Amazirh, A., Er-Raki, S., Chehbouni, A., Rivalland, V., Diarra, A., Khabba, S., Ezzahar, J., & Merlin, O. (2017). Modified Penman–Monteith equation for monitoring evapotranspiration of wheat crop:

688 Relationship between the surface resistance and remotely sensed stress index. *Biosystems*
689 *Engineering*, *164*(0), 68–84. https://doi.org/10.1016/j.biosystemseng.2017.09.015

690 Amazirh, A., Er-Raki, S., Ojha, N., Bouras, E. houssaine, Rivalland, V., Merlin, O., & Chehbouni, A.
691 (2022). Assimilation of SMAP disaggregated soil moisture and Landsat land surface temperature
692 to improve FAO-56 estimates of ET in semi-arid regions. Agricultural Water Management, 260.
693 https://doi.org/10.1016/j.agwat.2021.107290

694 Anapalli, S. S., Fisher, D. K., Pinnamaneni, S. R., & Reddy, K. N. (2020). Quantifying
695 evapotranspiration and crop coefficients for cotton (Gossypium hirsutum L.) using an eddy
696 covariance approach. *Agricultural Water Management*, *233*.
697 https://doi.org/10.1016/j.agwat.2020.106091

698 Anderson, M. C., Norman, J. M., Diak, G. R., Kustas, W. P., & Mecikalski, J. R. (1997). A two-source
699 time-integrated model for estimating surface fluxes using thermal infrared remote sensing. *Remote*
700 *Sensing of Environment*, *60*(2), 195–216. https://doi.org/10.1016/S0034-4257(96)00215-5

701 Anthoni, P. M., Law, B. E., Unsworth, M. H., & Vong, R. J. (2000). Variation of net radiation over
702 heterogeneous surfaces: Measurements and simulation in a juniper-sagebrush ecosystem.
703 *Agricultural and Forest Meteorology*. https://doi.org/10.1016/S0168-1923(00)00104-0

704 Aouade, G., Jarlan, L., Ezzahar, J., Er-raki, S., Napoly, A., Benkaddour, A., Khabba, S., Boulet, G.,
705 Garrigues, S., Chehbouni, A., & Boone, A. (2020). Evapotranspiration partition using the multiple
706 energy balance version of the ISBA-A-gs land surface model over two irrigated crops in a semi-
707 arid Mediterranean region (Marrakech, Morocco). Hydrol. Earth Syst. Sci., 24, 3789–3814, 2020.
708 https://doi.org/10.5194/hess-24-3789-2020

709 Bastiaanssen, W. G. M., Pelgrum, H., Wang, J., Ma, Y., Moreno, J. F., Roerink, G. J., & Van Der Wal,
710 T. (1998). A remote sensing surface energy balance algorithm for land (SEBAL): 2. Validation.
711 *Journal of Hydrology*, 213–229. https://doi.org/10.1016/S0022-1694(98)00254-6

712 Belaqziz, S., Khabba, S., Er-Raki, S., Jarlan, L., Le Page, M., Kharrou, M. H., Adnani, M. El, &
713 Chehbouni, A. (2013). A new irrigation priority index based on remote sensing data for assessing
714 the networks irrigation scheduling. *Agricultural Water Management*, *119*, 1–9.
715 https://doi.org/10.1016/j.agwat.2012.12.011

716 Blasch, K. W., & Bryson, J. R. (2007). Distinguishing sources of ground water recharge by using δ2H
717 and δ18O. *Ground Water*, *45*(3), 294–308. https://doi.org/10.1111/j.1745-6584.2006.00289.x

718 Bouimouass, H., Fakir, Y., Tweed, S., & Leblanc, M. (2020). Groundwater recharge sources in semiarid
719 irrigated mountain fronts. *Hydrological Processes*, *34*(7), 1598–1615.

https://doi.org/10.1002/hyp.13685

Boukhari, K., Fakir, Y., Stigter, T. Y., Hajhouji, Y., & Boulet, G. (2015). Origin of recharge and salinity and their role on management issues of a large alluvial aquifer system in the semi-arid Haouz plain, Morocco. *Environmental Earth Sciences*, *73*(10), 6195–6212. https://doi.org/10.1007/s12665-014-3844-y

Boulet, G., Braud, I., & Vauclin, M. (1997). Study of the mechanisms of evaporation under arid conditions using a detailed model of the soil-atmosphere continuum. Application to the EFEDA I experiment. *Journal of Hydrology*, *193*(1–4), 114–141. https://doi.org/10.1016/S0022-1694(96)03148-4

Boulet, G., Mougenot, B., Lhomme, J. P., Fanise, P., Lili-Chabaane, Z., Olioso, A., Bahir, M., Rivalland, V., Jarlan, L., Merlin, O., Coudert, B., Er-Raki, S., & Lagouarde, J. P. (2015). The SPARSE model for the prediction of water stress and evapotranspiration components from thermal infra-red data and its evaluation over irrigated and rainfed wheat. *Hydrology and Earth System Sciences*, 4653–4672. https://doi.org/10.5194/hess-19-4653-2015

Braud, I., Dantas-Antonino, A. C., Vauclin, M., Thony, J. L., and Ruelle, P. (1995). A simple soil-plant-atmosphere transfer model (SiSPAT) development and field verification, J. Hydrol., 166, 213–250. https://doi.org/10.1016/0022-1694(94)05085-C, 1995.

Brutsaert, W., & Kustas, W. P. (1987). Surface water vapor and momentum fluxes under unstable conditions from a rugged-complex area. *Journal of the Atmospheric Sciences*, *44*(2), 421–431. https://doi.org/10.1175/1520-0469(1987)044<0421:SWVAMF>2.0.CO;2

Byun, K., Liaqat, U. W., & Choi, M. (2014). Dual-model approaches for evapotranspiration analyses over homo- and heterogeneous land surface conditions. *Agricultural and Forest Meteorology*, *197*, 169–187. https://doi.org/10.1016/j.agrformet.2014.07.001

Chehbouni, A., Escadafal, R., Duchemin, B., Boulet, G., Simonneaux, V., Dedieu, G., Mougenot, B., Khabba, S., Kharrou, H., Maisongrande, P., Merlin, O., Chaponnière, A., Ezzahar, J., Er-Raki, S., Hoedjes, J., Hadria, R., Abourida, A., Cheggour, A., Raibi, F., … Sobrino, J. A. (2008). An integrated modelling and remote sensing approach for hydrological study in arid and semi-arid regions: The SUDMED programme. *International Journal of Remote Sensing*, *29*(17–18), 5161–5181. https://doi.org/10.1080/01431160802036417

Chirouze, J., Boulet, G., Jarlan, L., Fieuzal, R., Rodriguez, J. C., Ezzahar, J., Er-Raki, S., Bigeard, G., Merlin, O., Garatuza-Payan, J., Watts, C., & Chehbouni, G. (2014). Intercomparison of four remote-sensing-based energy balance methods to retrieve surface evapotranspiration and water stress of irrigated fields in semi-arid climate. *Hydrology and Earth System Sciences*, *18*(3), 1165–

1188. https://doi.org/10.5194/hess-18-1165-2014

Choudhury, B. J., Ahmed, N. U., Idso, S. B., Reginato, R.J., and Daughtry, C.S.T. (1994). Relations Between Evaporation Coefficients and Vegetation Indices Studied by Model simulations. Remote Sensing of Environment, 50:1-17.

Connor, D.J., Gómez-del-Campo, M., Comas, J. (2012). Yield characteristics of N–S oriented olive hedgerows, cv. Arbequina. Sci. Hortic. 133, 31–36. https://doi.org/10.1016/j.scienta.2011.10.008.

Courault, D., Bsaibes, A., Kpemlie, E., Hadria, R., Hagolle, O., Marloie, O., Hanocq, J. F., Olioso, A., Bertrand, N., & Desfonds, V. (2008). Assessing the potentialities of FORMOSAT-2 data for water and crop monitoring at small regional scale in South-Eastern France. *Sensors*, *8*, 3460–3481. https://doi.org/10.3390/s8053460

De Bruin H.A.R., Kohsiek W., van den Hurk B.J.J.M., (1993). A verification of some methods to determine the fluxes of momentum, sensible heat and water vapour using standard deviation and structure parameter of scalar meteorological quantities. Boundary Layer Meteorol 63: 231–257.

Delogu, E., Boulet, G., Olioso, A., Coudert, B., Chirouze, J., Ceschia, E., Le Dantec, V., Marloie, O., Chehbouni, G., & Lagouarde, J. P. (2012). Reconstruction of temporal variations of evapotranspiration using instantaneous estimates at the time of satellite overpass. *Hydrology and Earth System Sciences*, *16*, 2995–3010. https://doi.org/10.5194/hess-16-2995-2012

Delogu, Emilie, Boulet, G., Olioso, A., Garrigues, S., Brut, A., Tallec, T., Demarty, J., Soudani, K., & Lagouarde, J. P. (2018). Evaluation of the SPARSE dual-source model for predictingwater stress and evapotranspiration from thermal infrared data over multiple crops and climates. *Remote Sensing*, *10*(11). https://doi.org/10.3390/rs10111806

Diarra, A., Jarlan, L., Er-Raki, S., Le Page, M., Aouade, G., Tavernier, A., Boulet, G., Ezzahar, J., Merlin, O., & Khabba, S. (2017). Performance of the two-source energy budget (TSEB) model for the monitoring of evapotranspiration over irrigated annual crops in North Africa. *Agricultural Water Management*, *193*, 71–88. https://doi.org/10.1016/j.agwat.2017.08.007

Duchemin, B., Hadria, R., Erraki, S., Boulet, G., Maisongrande, P., Chehbouni, A., Escadafal, R., Ezzahar, J., Hoedjes, J. C. B., Kharrou, M. H., Khabba, S., Mougenot, B., Olioso, A., Rodriguez, J. C., & Simonneaux, V. (2006). Monitoring wheat phenology and irrigation in Central Morocco: On the use of relationships between evapotranspiration, crops coefficients, leaf area index and remotely-sensed vegetation indices. *Agricultural Water Management*, *79*, 1–27. https://doi.org/10.1016/j.agwat.2005.02.013

Duchemin, B., Hagolle, O., Mougenot, B., Simonneaux, V., Benhadj I., Hadria, R., Ezzahar, J., Hoedjes,

J., Khabba, S., Kharrou, M.H, Boulet, G., Dedieu, G., Er-Raki, S., Escadafal, R., Olioso, A., Chehbouni, A.G. (2008). Agrometerological study of semi-arid areas: an experiment for analysing the potential of FORMOSAT-2 time series of images in the Tensift-Marrakech plain. International Journal of Remote Sensing, 29: 5291-5299.

Elfarkh, J., Er-Raki, S., Ezzahar, J., Chehbouni, A., Aithssaine, B., Amazirh, A., Khabba, S., & Jarlan, L. (2021). Integrating thermal stress indexes within Shuttleworth–Wallace model for evapotranspiration mapping over a complex surface. *Irrigation Science*, *39*(1), 45–61. https://doi.org/10.1007/s00271-020-00701-3

Elfarkh, J., Ezzahar, J., Er-raki, S., Simonneaux, V., Hssaine, B. A., Rachidi, S., Brut, A., Vincent, R., & Khabba, S. (2020). Multi-Scale Evaluation of the TSEB Model over a Complex Agricultural Landscape in Morocco. *Remote Sensing*, *1*. https://doi.org/10.3390/rs12071181

Er-Raki, S., Chehbouni, A., Boulet, G., & Williams, D. G. (2010). Using the dual approach of FAO-56 for partitioning ET into soil and plant components for olive orchards in a semi-arid region. *Agricultural Water Management*, *97*(11), 1769–1778. https://doi.org/10.1016/j.agwat.2010.06.009

Er-Raki, S., Chehbouni, A., Guemouria, N., Duchemin, B., Ezzahar, J., & Hadria, R. (2007). Combining FAO-56 model and ground-based remote sensing to estimate water consumptions of wheat crops in a semi-arid region. *Agricultural Water Management*, *87*, 41–54. https://doi.org/10.1016/j.agwat.2006.02.004

Er-Raki, S., Ezzahar, J., Khabba, S., Jarlan, L., Kharrou, M. H., & Chehbouni, G. (2013). Micrometeorology tools for measuring evapotranspiration from the leaf to the region. In *Evapotranspiration: Processes, Sources and Environmental Implications* (pp. 1–22). Nova Science Publishers, Inc.

Ezzahar, J., Chehbouni, A., Er-Raki, S., & Hanich, L. (2009a). Combining a large aperture scintillometer and estimates of available energy to derive evapotranspiration over several agricultural fields in a semi-arid region. *Plant Biosystems*, *143*, 209–221. https://doi.org/10.1080/11263500802710036

Ezzahar, J., Chehbouni, A., Hoedjes, J. C. B., Er-Raki, S., Chehbouni, A., Boulet, G., Bonnefond, J. M., & De Bruin, H. A. R. (2007a). The use of the scintillation technique for monitoring seasonal water consumption of olive orchards in a semi-arid region. *Agricultural Water Management*, *89*(3), 173–184. https://doi.org/10.1016/j.agwat.2006.12.015

Ezzahar, J., Chehbouni, A., Hoedjes, J. C. B., & Chehbouni, A. (2007b). On the application of scintillometry over heterogeneous grids. *Journal of Hydrology*, *334*(3–4), 493–501. https://doi.org/10.1016/j.jhydrol.2006.10.027

Ezzahar, J., Chehbouni, A., Hoedjes, J., Ramier, D., Boulain, N., Boubkraoui, S., Cappelaere, B., Descroix, L., Mougenot, B., & Timouk, F. (2009b). Combining scintillometer measurements and an aggregation scheme to estimate area-averaged latent heat flux during the AMMA experiment. *Journal of Hydrology*, *375*(1–2), 217–226. https://doi.org/10.1016/j.jhydrol.2009.01.010

Ezzahar, J.; Chehbouni, A. (2009c). The use of scintillometry for validating aggregation schemes over heterogeneous grids. Agricultural and Forest Meteorology, 149, 2098–2109. https://doi.org/10.1016/j.agrformet.2009.09.004

Fang, B., Lei, H., Zhang, Y., Quan, Q., & Yang, D. (2020). Spatio-temporal patterns of evapotranspiration based on upscaling eddy covariance measurements in the dryland of the North China Plain. *Agricultural and Forest Meteorology*, *281*. https://doi.org/10.1016/j.agrformet.2019.107844

Fernández J. E., 2014. Understanding olive adaptation to abiotic stresses as a tool to increase crop performance. Environmental and Experimental Botany. 103 158-179.

Gallego-Elvira, B., Olioso, A., Mira, M., Castillo, S. R.-, Boulet, G., Marloie, O., Garrigues, S., Courault, D., Weiss, M., Chauvelon, P., & Boutron, O. (2013). EVASPA (EVapotranspiration Assessment from SPAce) Tool: An overview. *Procedia Environmental Sciences*, *19*, 303–310. https://doi.org/10.1016/j.proenv.2013.06.035

Gentine, P., Entekhabi, D., Chehbouni, A., Boulet, G., & Duchemin, B. (2007). Analysis of evaporative fraction diurnal behaviour. *Agricultural and Forest Meteorology*, *143*(1–2), 13–29. https://doi.org/10.1016/j.agrformet.2006.11.002

Hartogensis, O. K., Watts, C. J., Rodriguez, J.-C., & De Bruin, H. a. R. (2003). Derivation of an Effective Height for Scintillometers: La Poza Experiment in Northwest Mexico. *Journal of Hydrometeorology*, *4*(5), 915–928. https://doi.org/10.1175/1525-7541(2003)004<0915:DOAEHF>2.0.CO;2

Hoedjes, J.C.B., Chehbouni, A., Jacob, F., Ezzahar, J., & Boulet, G. (2008). Deriving daily evapotranspiration from remotely sensed instantaneous evaporative fraction over olive orchard in semi-arid Morocco. *Journal of Hydrology*, *354*(1–4), 53–64. https://doi.org/10.1016/j.jhydrol.2008.02.016

Horst, T. W., & Weil, J. C. (1992). Footprint estimation for scalar flux measurements in the atmospheric surface layer. *Boundary-Layer Meteorology*, *59*(3), 279–296. https://doi.org/10.1007/BF00119817

Hssaine, B. A., Ezzahar, J., Jarlan, L., Merlin, O., Khabba, S., Brut, A., Er-Raki, S., Elfarkh, J.,

Cappelaere, B., & Chehbouni, G. (2018). Combining a two source energy balance model driven by MODIS and MSG-SEVIRI products with an aggregation approach to estimate turbulent fluxes over sparse and heterogeneous vegetation in Sahel region (Niger). *Remote Sensing*, *10*(6). https://doi.org/10.3390/rs10060974

Hssaine, B. A., Merlin, O., Rafi, Z., Ezzahar, J., Jarlan, L., Khabba, S., & Er-Raki, S. (2018). Calibrating an evapotranspiration model using radiometric surface temperature, vegetation cover fraction and near-surface soil moisture data. *Agricultural and Forest Meteorology*, *256–257*(August 2017), 104–115. https://doi.org/10.1016/j.agrformet.2018.02.033

Hu, Z., Yu, G., Zhou, Y., Sun, X., Li, Y., Shi, P., Wang, Y., Song, X., Zheng, Z., Zhang, L., & Li, S. (2009). Partitioning of evapotranspiration and its controls in four grassland ecosystems: Application of a two-source model. *Agricultural and Forest Meteorology*, *149*(9), 1410–1420. https://doi.org/10.1016/j.agrformet.2009.03.014

Isabelle, P. E., Nadeau, D. F., Perelet, A. O., Pardyjak, E. R., Rousseau, A. N., & Anctil, F. (2020). Application and Evaluation of a Two-Wavelength Scintillometry System for Operation in a Complex Shallow Boreal-Forested Valley. *Boundary-Layer Meteorology*, *174*, 341–370. https://doi.org/10.1007/s10546-019-00488-7

Jackson, R. D., Moran, M. S., Gay, L. W., & Raymond, L. H. (1987). Evaluating evaporation from field crops using airborne radiometry and ground-based meteorological data. *Irrigation Science*, *8*(2), 81–90. https://doi.org/10.1007/BF00259473

Kalma, J. D., McVicar, T. R., & McCabe, M. F. (2008). Estimating land surface evaporation: A review of methods using remotely sensed surface temperature data. *Surveys in Geophysics*, *29*(4–5), 421–469. https://doi.org/10.1007/s10712-008-9037-z

Kustas, W. P. (1990). Estimates of evapotranspiration with a one- and two-layer model of heat transfer over partial canopy cover. *Journal of Applied Meteorology*, *29*(8), 704–715. https://doi.org/10.1175/1520-0450(1990)029<0704:EOEWAO>2.0.CO;2

Kustas, W.P., Daughtry, C.S.T., Van Oevelen, P.J., (1993). Analytical treatment of the relationships between soil heat flux/net radiation ratio and vegetation indices. Remote Sensing of Environment, 46, 319–330.

Kustas, W. P., & Norman, J. M. (1996). Use of remote sensing for evapotranspiration monitoring over land surfaces. *Hydrological Sciences Journal*, *41*, 495–516. https://doi.org/10.1080/02626669609491522

Kustas, William P., & Norman, J. M. (1999). Evaluation of soil and vegetation heat flux predictions

using a simple two-source model with radiometric temperatures for partial canopy cover. *Agricultural and Forest Meteorology*, *94*(1), 13–29. https://doi.org/10.1016/S0168-1923(99)00005-2

Lagouarde, J. P., Bhattacharya, B. K., Crébassol, P., Gamet, P., Babu, S. S., Boulet, G., Briottet, X., Buddhiraju, K. M., Cherchali, S., Dadou, I., Dedieu, G., Gouhier, M., Hagolle, O., Irvine, M., Jacob, F., Kumar, A., Kumar, K. K., Laignel, B., Mallick, K., … Ramakrishnan, R. (2018). The Indian-French Trishna mission: Earth observation in the thermal infrared with high spatio-temporal resolution. *International Geoscience and Remote Sensing Symposium (IGARSS)*, 4078–4081. https://doi.org/10.1109/IGARSS.2018.8518720

Lavee, S., 1996. Biology and physiology of the olive tree. In: Lavee, S., Barranco, D., Bongi, G., Jardak, T., Loussert, R., Martin, G.C., Trigui, A. (Eds.), World Olive Encyclopaedia. International Olive Council, Madrid, Spain, pp. 61–110.

Le Page, M., Berjamy, B., Fakir, Y., Bourgin, F., Jarlan, L., Abourida, A., Benrhanem, M., Jacob, G., Huber, M., Sghrer, F., Simonneaux, V., & Chehbouni, G. (2012). An Integrated DSS for Groundwater Management Based on Remote Sensing. The Case of a Semi-arid Aquifer in Morocco. *Water Resources Management*, *26*(11), 3209–3230. https://doi.org/10.1007/s11269-012-0068-3

Li, Z. L., Tang, R., Wan, Z., Bi, Y., Zhou, C., Tang, B., Yan, G., & Zhang, X. (2009). A review of current methodologies for regional Evapotranspiration estimation from remotely sensed data. In *Sensors* (pp. 3801–3853). https://doi.org/10.3390/s90503801

Liu, Y., & Yamanaka, T. (2012). Tracing groundwater recharge sources in a mountain-plain transitional area using stable isotopes and hydrochemistry. *Journal of Hydrology*, *464–465*, 116–126. https://doi.org/10.1016/j.jhydrol.2012.06.053

Martinez, J. L., Raiber, M., & Cendón, D. I. (2017). Using 3D geological modelling and geochemical mixing models to characterise alluvial aquifer recharge sources in the upper Condamine River catchment, Queensland, Australia. *Science of the Total Environment*, *574*, 1–18. https://doi.org/10.1016/j.scitotenv.2016.09.029

Meijninger, W. M. L. (2003). Surface fluxes over natural landscapes using scintillometry. In *Wageningen UR publication*.

Montes, C., Lhomme, J. P., Demarty, J. Ô., Prévot, L., & Jacob, F. (2014). A three-source SVAT modeling of evaporation: Application to the seasonal dynamics of a grassed vineyard. *Agricultural and Forest Meteorology*, *191*, 64–80. https://doi.org/10.1016/j.agrformet.2014.02.004

Morillas, L., Leuning, R., Villagarcía, L., García, M., Serrano-Ortiz, P., & Domingo, F. (2013). Improving evapotranspiration estimates in Mediterranean drylands: The role of soil evaporation. *Water Resources Research*, *49*(10), 6572–6586. https://doi.org/10.1002/wrcr.20468

Norman, J. M., Kustas, W. P., & Humes, K. S. (1995). Source approach for estimating soil and vegetation energy fluxes in observations of directional radiometric surface temperature. *Agricultural and Forest Meteorology*, *77*(3–4), 263–293. https://doi.org/10.1016/0168-1923(95)02265-Y

Olioso, A., Chauki, H., Courault, D., & Wigneron, J. P. (1999). Estimation of evapotranspiration and photosynthesis by assimilation of remote sensing data into SVAT models. *Remote Sensing of Environment*, *68*(3), 341–356. https://doi.org/10.1016/S0034-4257(98)00121-7

Ouaadi, N., Jarlan, L., Ezzahar, J., Zribi, M., Khabba, S., Bouras, E., Bousbih, S., & Frison, P. L. (2020). Monitoring of wheat crops using the backscattering coefficient and the interferometric coherence derived from Sentinel-1 in semi-arid areas. *Remote Sensing of Environment*, *251*(15). https://doi.org/10.1016/j.rse.2020.112050

Parastatidis, D., Mitraka, Z., Chrysoulakis, N., & Abrams, M. (2017). Online global land surface temperature estimation from landsat. *Remote Sensing*, *9*(12). https://doi.org/10.3390/rs9121208

Rafi, Z., Merlin, O., Le Dantec, V., Khabba, S., Mordelet, P., Er-Raki, S., Amazirh, A., Olivera-Guerra, L., Ait Hssaine, B., Simonneaux, V., Ezzahar, J., & Ferrer, F. (2019). Partitioning evapotranspiration of a drip-irrigated wheat crop: Inter-comparing eddy covariance-, sap flow-, lysimeter- and FAO-based methods. *Agricultural and Forest Meteorology*, *265*, 310–326. https://doi.org/10.1016/j.agrformet.2018.11.031

Rannik, U., Aubinet, M., Kurbanmuradov, O., Sabelfeld, K. K., Markkanen, T., & Vesala, T. (2000). Footprint analysis for measurements over a heterogeneous forest. *Boundary-Layer Meteorology*, *97*(1), 137–166. https://doi.org/10.1023/A:1002702810929

Roerink, G. J., Su, Z., & Menenti, M. (2000). S-SEBI: A simple remote sensing algorithm to estimate the surface energy balance. *Physics and Chemistry of the Earth, Part B: Hydrology, Oceans and Atmosphere*, *25*(2), 147–157. https://doi.org/10.1016/S1464-1909(99)00128-8

Ryu, Y., Baldocchi, D. D., Black, T. A., Detto, M., Law, B. E., Leuning, R., Miyata, A., Reichstein, M., Vargas, R., Ammann, C., Beringer, J., Flanagan, L. B., Gu, L., Hutley, L. B., Kim, J., McCaughey, H., Moors, E. J., Rambal, S., & Vesala, T. (2012). On the temporal upscaling of evapotranspiration from instantaneous remote sensing measurements to 8-day mean daily-sums. *Agricultural and Forest Meteorology*, *152*(1), 212–222. https://doi.org/10.1016/j.agrformet.2011.09.010

946 Saadi, S., Boulet, G., Bahir, M., Brut, A., Delogu, É., Fanise, P., Mougenot, B., Simonneaux, V., &
947 Chabaane, Z. L. (2018). Assessment of actual evapotranspiration over a semiarid heterogeneous
948 land surface by means of coupled low-resolution remote sensing data with an energy balance
949 model: Comparison to extra-large aperture scintillometer measurements. *Hydrology and Earth*
950 *System Sciences*, *22*(4), 2187–2209. https://doi.org/10.5194/hess-22-2187-2018

951 Saadi, S., Simonneaux, V., Boulet, G., Raimbault, B., Mougenot, B., Fanise, P., Ayari, H., & Lili-
952 Chabaane, Z. (2015). Monitoring irrigation consumption using high resolution NDVI image time
953 series: Calibration and validation in the Kairouan plain (Tunisia). *Remote Sensing*, *7*(10), 13005–
954 13028. https://doi.org/10.3390/rs71013005

955 Sánchez, J. M., López-Urrea, R., Valentín, F., Caselles, V., & Galve, J. M. (2019). Lysimeter assessment
956 of the Simplified Two-Source Energy Balance model and eddy covariance system to estimate
957 vineyard evapotranspiration. *Agricultural and Forest Meteorology*, *274*, 172–183.
958 https://doi.org/10.1016/j.agrformet.2019.05.006

959 Schuepp, P. H., Leclerc, M. Y., MacPherson, J. I., & Desjardins, R. L. (1990). Footprint prediction of
960 scalar fluxes from analytical solutions of the diffusion equation. *Boundary-Layer Meteorology*,
961 *50*(1–4), 355–373. https://doi.org/10.1007/BF00120530

962 Shuttleworth, W. J. (1989). FIFE: The variation in energy partition at surface flux sites. *IAHS. Third Int*,
963 67–74.

964 Shuttleworth, W. James, & Wallace, J. S. (1985). Evaporation from sparse crops-an energy combination
965 theory. *The Quarterly Journal of the Royal Meteorological Society*, *111*(465), 839–855.
966 https://doi.org/10.1002/qj.49711146510

967 Simonneaux, V, Thomas, S., Lepage, M., Duchemin, B., Kharrou, M. H., Berjamy, B., Boulet, G., &
968 Chehbouni, G. (2007). «SAMIR», A tool for irrigation monitoring using remote sensing for
969 landcover mapping and evapotranspiration estimates. *2nd International Symposium on Recent*
970 *Advances in Quantitative Remote Sensing*, *2*(1), 597–601.
971 http://www.iwra.org/congress/2008/resource/authors/abs642_article.pdf

972 Simonneaux, Vincent, Lepage, M., Helson, D., Metral, J., Thomas, S., Duchemin, B., Cherkaoui, M.,
973 Kharrou, H., Berjami, B., & Chehbouni, A. (2009). Spatialized estimates of evapotranspiration of
974 irrigated crops using remote sensing: Application to irrigation management in the Haouz plain
975 (Marrakech, Morocco). *Secheresse (Montrouge)*, *20*(1), 123–130.

976 Sobrino, J. A., Jiménez-Muñoz, J. C., & Paolini, L. (2004). Land surface temperature retrieval from
977 LANDSAT TM 5. *Remote Sensing of Environment*, *90*, 434–440.
978 https://doi.org/10.1016/j.rse.2004.02.003

Srinet R., Nandy S., Patel N.R. (2019). Estimating leaf area index and light extinction coefficient using Random Forest regression algorithm in a tropical moist deciduous forest, India. Ecological Informatics, 52, 94-102. https://doi.org/10.1016/j.ecoinf.2019.05.008.

Su, Z. (2002). The Surface Energy Balance System (SEBS) for estimation of turbulent heat fluxes. *Hydrology and Earth System Sciences*, *6*(1), 85–100. https://doi.org/10.5194/hess-6-85-2002

Tardy, B., Rivalland, V., Huc, M., Hagolle, O., Marcq, S., & Boulet, G. (2016). A software tool for atmospheric correction and surface temperature estimation of Landsat infrared thermal data. *Remote Sensing*, *8*(9). https://doi.org/10.3390/rs8090696

Tasumi, M. (2019). Estimating evapotranspiration using METRIC model and Landsat data for better understandings of regional hydrology in the western Urmia Lake Basin. *Agricultural Water Management*, *226*. https://doi.org/10.1016/j.agwat.2019.105805

Torres, E. A., & Calera, A. (2010). Bare soil evaporation under high evaporation demand: a proposed modification to the FAO-56 model. *Hydrological Sciences Journal*, *55*(3), 303–315. https://doi.org/10.1080/02626661003683249

Tucker, C.J., (1979). Red and photographic infrared linear combinations for monitoring vegetation. Remote Sens Environ 8:127-150.

Twine, T. E., Kustas, W. P., Norman, J. M., Cook, D. R., Houser, P. R., Meyers, T. P., Prueger, J. H., Starks, P. J., & Wesely, M. L. (2000). Correcting eddy-covariance flux underestimates over a grassland. *Agricultural and Forest Meteorology*, *103*(3), 279–300. https://doi.org/10.1016/S0168-1923(00)00123-4

Van Dijk, A., Moene, A.F., De Bruin, H.A.R. (2004). The principles of surface flux physics: theory, practice and description of the ECPACK library, Internal report 2004/1, Meteorologyand Air Quality Group Wageningen University, pp. 97 (http://www.met.wur.nl/internal_reports/ir2004_01.pdf)

Van Niel, T. G., McVicar, T. R., Roderick, M. L., van Dijk, A. I. J. M., Renzullo, L. J., & van Gorsel, E. (2011). Correcting for systematic error in satellite-derived latent heat flux due to assumptions in temporal scaling: Assessment from flux tower observations. *Journal of Hydrology*, *409*(1–2), 140–148. https://doi.org/10.1016/j.jhydrol.2011.08.011

Wang, L., Parodi, G. N., & Su, Z. (2008). SEBS module beam: A practical tool for surface energy balance estimates from remote sensing data. *European Space Agency, (Special Publication) ESA SP*.

Wesely, ML., (1976) Combined effect of temperature and humidity fluctuations on refractive index. J Appl Meteorol 15:43–49. https://doi.org/10.1175/1520-0450(1976)015<0043:TCEOTA>2.0.CO;2

Widmoser, P., & Wohlfahrt, G. (2018). Attributing the energy imbalance by concurrent lysimeter and eddy covariance evapotranspiration measurements. *Agricultural and Forest Meteorology*, *263*, 287–291. https://doi.org/10.1016/j.agrformet.2018.09.003

Xu, T., Liu, S., Xu, L., Chen, Y., Jia, Z., Xu, Z., & Nielson, J. (2015). Temporal upscaling and reconstruction of thermal remotely sensed instantaneous evapotranspiration. *Remote Sensing*, *7*, 3400–3425. https://doi.org/10.3390/rs70303400

Zhao, J., Olivas, P. C., Kunwor, S., Malone, S. L., Staudhammer, C. L., Starr, G., & Oberbauer, S. F. (2018). Comparison of sensible heat flux measured by large aperture scintillometer and eddy covariance in a seasonally-inundated wetland. *Agricultural and Forest Meteorology*, *259*, 345–354. https://doi.org/10.1016/j.agrformet.2018.05.026

Zhu, G., Li, X., Su, Y., Zhang, K., Bai, Y., Ma, J., Li, C., Hu, X., & He, J. (2014). Simultaneously assimilating multivariate data sets into the two-source evapotranspiration model by Bayesian approach: application to spring maize in an arid region of northwestern China. Geoscientific Model Development, 7, 1467-1482. https://doi.org/10.5194/GMD-7-1467-2014

Zhu, G., Su, Y., Li, X., Zhang, K., & Li, C. (2013). Estimating actual evapotranspiration from an alpine grassland on Qinghai-Tibetan plateau using a two-source model and parameter uncertainty analysis by Bayesian approach. *Journal of Hydrology*, *476*, 42–51. https://doi.org/10.1016/j.jhydrol.2012.10.006